On the calculation of single-scattering properties of frozen droplets and frozen droplet aggregates observed in deep convective clouds

Jeonggyu Kim[1], Sungmin Park[1], Greg M. McFarquhar[2,3], Anthony J. Baran[4,5], Joo Wan Cha[6], Kyoungmi Lee[6], Seoung Soo Lee[7], Chang Hoon Jung[8], Kyo-Sun Sunny Lim[9], Junshik Um[1,10,11]

[1]BK21 School of Earth and Environmental Systems, Pusan National University, Busan, Republic of Korea

[2]Cooperative Institute for Severe and High Impact Weather Research and Operations, University of Oklahoma, Norman, Oklahoma, USA

[3]School of Meteorology, University of Oklahoma, Norman, Oklahoma, USA

[4]Department of Observation-Based Research, Met Office, Devon, Exeter, UK

[5][4]School of Physics, Astronomy, Mathematics, University of Hertfordshire, Hatfield, UK

[5]Department of Observation-Based Research, Met Office, Devon, Exeter, UK

[6]Meteorological Applied Research Department, National Institute of Meteorological Sciences, Seogwipo, Republic of Korea

[7]Earth System Science Interdisciplinary Center, University of Maryland, Maryland, USA

[8]Department of Health Management, Kyungin Women's University, Incheon, Republic of Korea

[9]Department of Atmospheric Sciences, Center for Atmospheric Remote Sensing, Kyungpook National University, Daegu, Republic of Korea.

[10]Department of Atmospheric Sciences, Pusan National University, Busan, Republic of Korea

[11]Institute of Environmental Studies, Pusan National University, Busan, Republic of Korea

Correspondence to: Junshik Um (jjunum@pusan.ac.kr)

Abstract. During multiple field campaigns, small quasi-spherical ice crystals, commonly referred to as frozen droplets (FDs), and their aggregates (frozen droplet aggregates (FDAs)), have been identified as the predominant habits in the upper regions of deep convective clouds (DCCs) and their associated anvils. These findings highlight the significance of FDs and FDAs for understanding the microphysics and radiative properties of DCCs. Despite the prevalence of FDs and FDAs at the tops of DCCs where they directly contribute to cloud radiative ~~forcing~~effect, the detailed single-scattering properties (e.g., scattering-phase function P_{11} and asymmetry parameter g) of FDs and FDAs remain highly uncertain. This uncertainty is mainly due to insufficient in situ measurements and the resolution of cloud probes, which hinder the development of idealized shape models for FDs and FDAs. In this study, two shape models, the Gaussian random sphere (GS) and droxtal (DX), are proposed as possible representations for the shapes of in-situ measured FDs and FDAs. A total of 120 individual models of GSs and 129 models of DXs were generated by varying their shapes. Furthermore, by attaching these individual models in both homogeneous or heterogeneous manners, three different types and a total of ~~404~~315 models of FDAs were created: (1) aggregates of GSs; (2) aggregates of DXs; and (3) combinations of GSs and DXs which are called habit mixtures (HMs). The P_{11} and g of the developed models were calculated using a geometric optics method at a wavelength of 0.80 μm and then compared with those obtained using a Polar Nephelometer (PN) during the CIRCLE−2 field campaign to assess the models. Both individual component ice crystals (i.e., either GS or DX) and homogeneous component aggregates (i.e., either aggregates of GSs or aggregates of DXs) showed substantial differences compared with the PN measurements, whereas the P_{11} of the HMs was found to match most accurately the in situ measured P_{11}, reducing the differences to ±0.87%, ±0.88%, and −5.37% in the forward, lateral, and backward scattering regions, respectively. The g of the HMs was found to be 0.80 which falls within the range of the PN measurement (0.78 ± 0.04). The root mean square error for the HM was minimized to a value of 0.0427. It was shown that the novel HMs developed in this study demonstrated better performance than in previous research where

HMs were developed indirectly by weighting the calculated P_{11} of shape models to interpret in situ measurement. The results of this study suggest potential~~carries important~~ implications for enhancing the calculation of single-scattering properties of ice crystals in DCCs.

1 Introduction

45 Deep convective clouds significantly influence the Earth's energy budget, hydrological cycle, and climate system (Jensen et al., 1996; de Reus et al., 2009; Frey et al., 2011; Gayet et al., 2012; Raymond and Blyth, 2016). Characterized by intense updrafts and towering vertical structures, these clouds play a crucial role in transporting heat, moisture, and momentum throughout the troposphere (Houze, 2014; Lee et al., 2019), as well as injecting water vapor into the stratosphere (Dauhut and Hohenegger, 2022). Vertical motions lift moist air, resulting in the formation of ice crystals and subsequent precipitation

50 (Andreae et al., 2004). Their radiative properties are crucial, affecting the Earth's radiative balance, through solar and terrestrial radiation interactions. Understanding these properties is vital for climate models and feedback mechanisms. Furthermore, deep convective clouds contribute to severe weather events, like thunderstorms, heavy rainfall, and lightning, impacting weather prediction and societal concerns (Williams, 2018). Therefore, investigating their radiative properties advances our comprehension of their atmospheric and climatic role, enhancing climate projections and weather forecasting.

55 Limited in situ observations have been made to characterize the microphysical and radiative properties of deep convective clouds, especially in convective cores, due to safety concerns related to the vigorous updrafts (> 15 m/s), which prevent penetrations of research aircraft into the cores. During the Cirrus Cloud Experiment (CIRCLE−2, Gayet et al., 2012), the Deep Convective Clouds and Chemistry (DC3, Barth et al., 2015), and the CapeEx19 (Nairy, 2022) field campaigns, the microphysical properties (e.g., size and habit distributions) of ice crystals at the upper levels of deep convective clouds were

60 measured. These upper regions of deep convective clouds were characterized by abundant quasi-spherical ice crystals, with maximum dimensions (D_{max}) smaller than ~50 μm (Heymsfield and Sabin, 1989; Phillips et al., 2007, Lawson et al., 2010; Järvinen et al., 2016), and their aggregates (Gayet et al., 2012; Baran et al., 2012; Stith et al., 2014; Järvinen et al., 2016; Um et al., 2018). The presence of small quasi-spherical frozen droplets (FDs) has been attributed to homogeneous freezing of supercooled droplets rapidly ascending in the updraft (Rosenfeld and Woodley, 2000; Gayet et al., 2012), whereas linear

65 "chain-like" shaped frozen droplet aggregates (FDAs) have been observed in environments with enhanced electric field (e.g., electrified thunderstorms) (Saunders and Wahab, 1975; Stith et al., 2002, 2004; Lawson et al., 2003; Connolly et al., 2005; Um and McFarquhar, 2009; Pedernera and Ávila, 2018; Um et al., 2018).

Gayet et al. (2012) observed FDs and FDAs in the overshooting tops of a continental deep convective cloud at a temperature of approximately −58 °C during CIRCLE−2 with unusually high concentrations of ice crystals up to 70 cm^{-3}. A dense cloud

70 top exhibited a mean effective diameter of ~43 μm and a maximum particle size of approximately 300 μm, whereas the average asymmetry parameter (g) was determined to be approximately 0.776 using a Polar Nephelometer (PN) (Crépel et al., 1997; Gayet et al., 1997). Um et al. (2018) further investigated the morphological characteristics of FDs and FDAs using cloud particle imager (CPI) data obtained during the DC3 field campaign. The CPI data were collected from the upper anvils of two storms at altitudes between 12.0 and 12.4 km, at temperatures (T) ranging from −61 to −55 °C. It was revealed that FDs and

75 FDAs were the predominant habits, comprising 93.9~~73.0~~ % (by number) and 86.3~~46.3~~ % (by projected area) of the observed particles, respectively. The average number (4.7 ± 5.0), size (31.79 ± 7.12 μm), and relative position of element FDs comprising the FDAs were also determined (Um et al., 2018).

To quantify the radiative impacts of deep convective clouds, calculations of single-scattering properties of constituent ice crystals are required, and idealized models representing realistic shapes of these constituent ice crystals should be developed.

80 The assumption of spherical shapes for the element FDs within FDAs was made to quantify the morphological characteristics of FDs and FDAs by Um et al. (2018). This assumption is valid for determining the size (i.e., D_{max}) and the relative position

between FDs within FDAs, but it is not suitable for calculating the single-scattering properties (e.g., scattering-phase function P_{11} and g) of non-spherically shaped FDs (Um and McFarquhar, 2011).

Even though a high resolution (i.e., 2.3 μm) CPI was used during the CIRCLE−2 (Gayet et al., 2012) and DC3 (Stith et al., 2014) campaigns to image FDs its resolution was not sufficiently high to fully resolve the three-dimensional morphological features (e.g., non-sphericity and surface roughness) of FDs. This limitation introduces uncertainties in the calculations of single-scattering properties (Um and McFarquhar, 2011). In contrast, the FDs and FDAs imaged by the particle habit imaging and polar scattering (PHIPS, Abdelmonem et al., 2016) probe during the CapeEx19 campaign showed distinct non-spherical, plate-like shapes (Nairy, 2022). On the other hand, FDs captured in the vicinity of the convective core using the Ice Cryo−Encapsulation by Balloon (ICE−Ball) system showed quasi-spherical shapes with pronounced surface roughness (Magee et al., 2021). Laboratory−grown FDs and FDAs have also shown both quasi-spherical and non-spherical shapes of FDs (Pedernera and Ávila, 2018).

Given the uncertainties surrounding the shapes of observed FDs and small ice crystals, several idealized shape models have been proposed to better represent the quasi-spherical nature of FDs and small ice crystals (Jang et al., 2022). These models include the Gaussian random sphere (Muinonen et al., 1996), droxtal (Yang et al., 2003), budding Bucky ball (Um et al., 2011), and Chebyshev particle (Mugnai and Wiscombe, 1980; McFarquhar et al., 2002; Um and McFarquhar, 2011; Baran et al., 2012). In particular, two methods, the Gaussian random sphere and droxtal, produce shapes that closely resemble those observed in field campaigns and experiments (Thuman and Robinson, 1954; Othake, 1970; Yamazaki and Gonda, 1984; Pedernera and Ávila, 2018; Magee et al., 2021). The Gaussian random sphere is well-suited to describe FDs composed of roughened facets, while experiments conducted in a cold cloud chamber at temperatures below −40 °C suggest that the shapes of FDs more closely resemble those of droxtals (see Figs. 2−3 of Pedernera and Ávila, 2018). Although Baran et al. (2012) applied a weighted habit mixture model of Chebyshev particles and hexagonal ice aggregates to calculate the single-scattering properties of FDAs, the development of idealized models specifically for FDAs and direct calculations of their single-scattering properties has yet to be thoroughly explored.

In this study, idealized shape models were developed using Gaussian random spheres and droxtals to represent the shapes of FDs and FDAs and the corresponding single-scattering properties were computed using a geometric optics method. The results of these theoretical calculations are then compared with in situ measurements obtained during CIRCLE−2 to evaluate the developed models. The remainder of this paper is organized into the following sections: Section 2 outlines the development of shape models for FDs and FDAs based on in situ measurements. Section 3 details the theoretical methodology used to calculate the single-scattering properties of FDs and FDAs. Section 4 discusses the results, and Section 5 provides a summary and conclusion of this study.

2 Idealized models representing the shapes of frozen droplets and frozen droplet aggregates

To compute the single-scattering properties of FDs and FDAs, it is essential to have idealized shape models that closely replicate their natural form. In this study, ~~shape models representing quasi-spherical FDs and FDAs~~ these models were developed using Gaussian random spheres and droxtals. based on the shapes ~~of these particles~~ observed during field campaigns and laboratory experiments. This section presents the geometrical description of the Gaussian random sphere and droxtal. Additionally, it outlines the procedure used to construct shape models of FDAs.

2.1 Gaussian random sphere

The Gaussian random sphere is widely used to depict natural particles characterized by uneven surfaces, such as asteroids (Muinonen and Lagerros, 1998), desert dust particles (Nousiainen et al., 2003), and small ice crystals (Nousiainen and McFarquhar, 2004; Nousiainen et al., 2011). Magee et al. (2021) recently revealed previously undiscovered uneven and rough

surfaces due to the limited resolution of imaging probes. Therefore, the Gaussian random sphere is well-suitable for generating models to represent FDs because it is designed to represent uneven and rough surfaces. Here, idealized models of FDs, represented by Gaussian random spheres, were developed using the SIRIS software (Muinonen et al., 1996; Nousiainen et al., 2003). This software enables the generation of quasi-spherical shapes with randomly deformed surfaces through the utilization of Gaussian random sphere geometry along with several statistical parameters.

Two statistical parameters, the relative standard deviation of radius (σ) and correlation angle (Γ), were varied to generate a total of 120 Gaussian random spheres. 20 different Γ (i.e., from 0.01 to 0.20) were used to develop each case of Gaussian random spheres. Adjusting σ affects the radius vector (Υ) of the Gaussian random sphere and the radius vector is defined in spherical coordinates as

$$\Upsilon(\vartheta, \varphi) = \frac{a}{\sqrt{1+\sigma^2}} \exp[s(\vartheta, \varphi)] \hat{e_r} \text{ and} \qquad (1)$$

$$s(\vartheta, \varphi) = \sum_{l=0}^{\infty} \sum_{m=-l}^{l} s_{lm} Y_{lm}(\vartheta, \varphi), \qquad (2)$$

where a denotes the mean radius, Y_{lm} is the orthonormal spherical harmonics, and s_{lm} is a Gaussian random variable generated with zero means (Muinonen et al., 2007). The s and $\hat{e_r}$ is logradius and a unit vector pointing outward in the direction (ϑ, φ) in spherical coordinates, respectively. The Γ is correlation angle which is defined by

$$\Gamma = 2\arcsin\left(\frac{1}{2}l\right) \text{ and} \qquad (3)$$

$$C_s(r) = exp\left(-\frac{2}{l^2} sin^2 \frac{1}{2} r\right), \qquad (4)$$

where C_s is the correlation function and l is the correlation length (Nousiainen, 2002). Table 1 lists the values of these statistical parameters used to generate the Gaussian random spheres. Figure 1 shows example realizations of the geometric shapes of Gaussian random spheres with $D_{max} = 30$ μm. As Γ decreases while σ remains constant (i.e., from Fig. 1f to 1a), the shapes of Gaussian random spheres progressively deviate from a spherical form, assuming an increasingly spiky and appearance not like those of observed ice crystals. More detailed information on the SIRIS software and Gaussian random sphere geometry can be found in Muinonen et al. (1996) and Nousiainen et al. (2003).

Table 1. Statistical parameters, Γ and σ, used to develop six cases of FDs represented by Gaussian random spheres are shown.

case	1	2	3	4	5	6
Γ	10°	20°	30°	60°	90°	180°
σ			0.01 ~ 0.20			
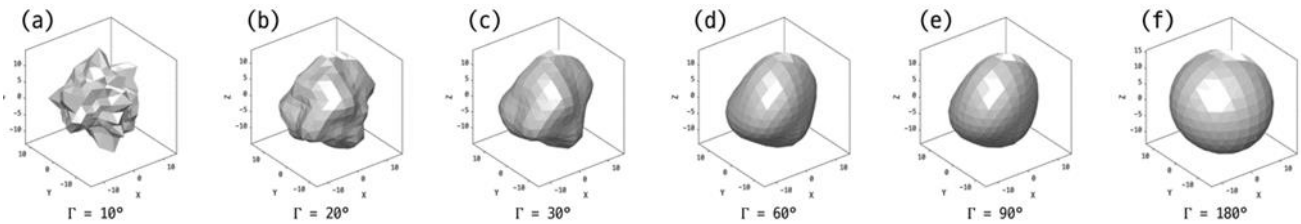
Figure 1. Example realizations of the Gaussian random spheres based on six different Γ. The σ is 0.15 for all the cases presented here and the values of Γ for each model are embedded at the bottom of each panel. The D_{max} of Gaussian random spheres is identical (i.e., 30 μm) for all the cases.
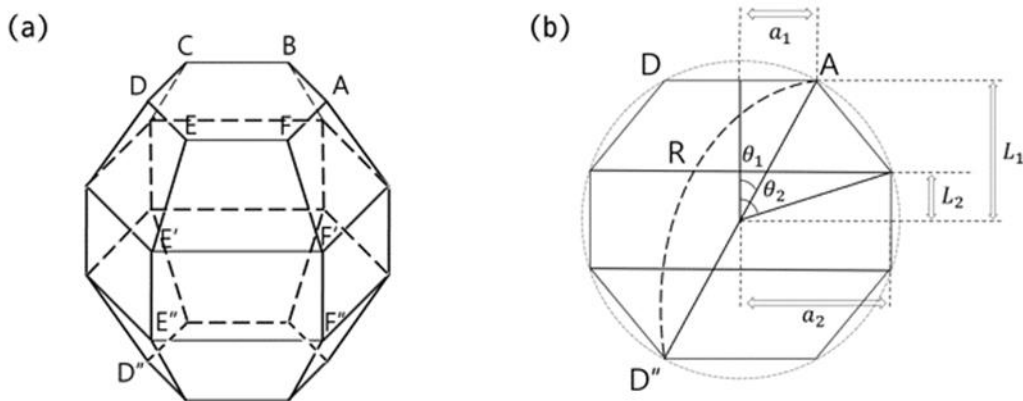
2.2 Droxtal

155 Thuman and Robinson (1954) researched Alaskan ice fog, collecting ice crystals using glass slides. They discovered unusual, small ice particles that exhibited characteristics of both droplets and crystals at temperatures less than –35 °C. These particles were more prevalent than the well-formed hexagonal columns and plates typically expected. The researchers named these unique ice particles as droxtals. Later, Othake (1970) identified droxtals as 14 or 20−faced polyhedral crystals, noting that such particles are no longer considered unusual in ice fog conditions. Yamazaki and Gonda (1984) advanced this understanding

160 by demonstrating the growth of a 20−faceted ice crystal from a frozen droplet through their experiments (see their Fig.1). The droxtals were used to calculate single-scattering properties of small quasi-ice crystals observed in cirrus clouds using the finite-difference time domain method (Yang et al., 2003) and the improved geometric optics method (Zhang et al., 2004).

For $T < –40$ °C, cloud droplets freeze so rapidly that they do not have sufficient time to develop into typical shapes, such as hexagonal columns (Ohtake, 1970). Recent laboratory results reported that FDs observed at temperatures less than −40 °C

165 bear a resemblance to the shape of droxtals (Pedernera and Ávila, 2018). Considering the aforementioned observations and experiments, it is plausible to assume the droxtal geometry as a possible candidate representing the shape of small and quasi-spherical ice crystals which are observed in the upper anvil of DCCs.

Figure 2 shows the geometrical configuration of a droxtal. Two angular parameters θ_1 and θ_2, in conjunction with the radius (R) of a circumscribing sphere, determine the geometry of the droxtal. The relationships of these parameters are given by:
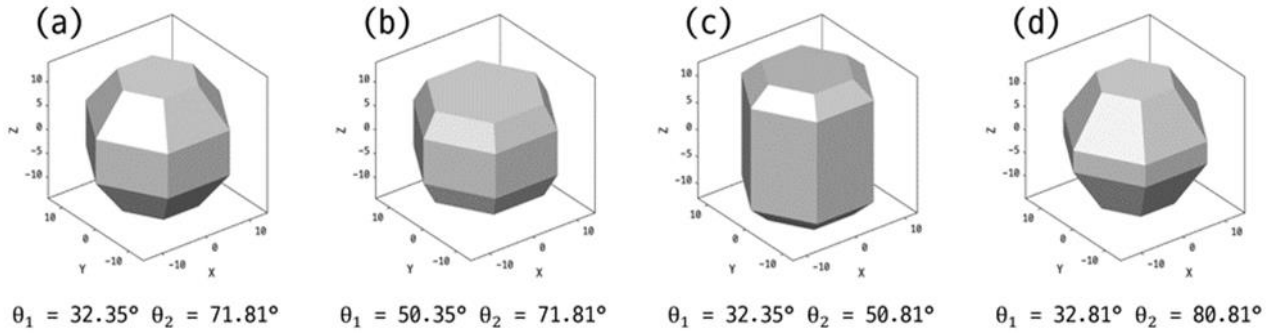
170 $a_1 = R sin\theta_1$ and $a_2 = R sin\theta_2$ and (5)

$L_1 = R cos\theta_1$ and $L_2 = R cos\theta_2$ and (6)

where a_1 and a_2 are connected with the area of hexagonal faces of the droxtal. In Eq. (6), L_1 and L_2 are related to the area of rectangular and trapezoidal faces, respectively. With a total of 20 faces, a single droxtal features 12 trapezoidal faces (e.g., EFF'E' in Fig. 2a), 6 rectangular faces (e.g., E'F'F''E'' in Fig. 2a), and 2 hexagonal faces (e.g., ABCDEF in Fig. 2a). The

175 single droxtal, specified by $\theta_1 = 32.35°$ and $\theta_2 = 71.81°$, exhibits maximum sphericity. Based on this model representing maximum sphericity, modifications were made to generate the idealized droxtal models. By adjusting either θ_1 or θ_2 at one-degree intervals, a total of 12~~7~~9 idealized droxtal models with $D_{max} = 30$ μm were developed. Four example realizations of the droxtal are illustrated in Fig. 3. Figures 3a and 3b correspond to the case where θ_1 varies, while θ_2 is fixed at 71.81°. Conversely, Figs. 3c and 3d show the cases where θ_2 is varied, while θ_1 is held constant at 32.35°. The corresponding values of θ_1 and θ_2

180 are shown at the bottom of each panel. Table 2 gives the values and ranges of the angular parameters for each droxtal case developed in this study.

185 **Figure 2. Geometrical configuration of a droxtal. The $\overline{AD''}$ in (b) corresponds to the maximum dimension (D_{max}). Adjusting the two angles, θ_1 and θ_2, influences the area of hexagonal, rectangular, and trapezoidal faces of droxtal.**

5

$\theta_1 = 32.35° \quad \theta_2 = 71.81° \qquad \theta_1 = 50.35° \quad \theta_2 = 71.81° \qquad \theta_1 = 32.35° \quad \theta_2 = 50.81° \qquad \theta_1 = 32.81° \quad \theta_2 = 80.81°$

Figure 3. Example realizations of droxtal models based on the four cases shape statistics. The D_{max} for each droxtal model is 30 μm. Corresponding statistical parameters, θ_1 and θ_2, are shown at the bottom of each panel.

Table 2. Statistical parameters, θ_1 and θ_2, used to develop four cases of FDs represented by droxtals are shown.

case	1	2	3	4
θ_1	1.35° ~ 32.35°	33.35° ~ 71.35°	32.35°	32.35°
θ_2	71.81°	71.81°	32.81° ~ 71.81°	72.81° ~ 89.81°

2.3 Frozen droplet aggregates

Linearly-chained FDAs are one of the distinct characteristics of continental DCCs, which may be produced by high electric fields that exist within the clouds (Saunders and Wahab, 1975; Stith et al., 2002, 2004, 2014; Connolly et al., 2005; Gayet et al., 2012; Järvinen et al., 2016; Um et al., 2018). According to an analysis on the morphological properties of FDAs by Um et al. (2018), on average, FDAs consisted of 4.7 ± 5.0 individual FDs, with approximately 90 % of the measured FDAs being composed of 2 to 10 individual FDs.

In this section, idealized models representing the linearly-chained and complex shapes of FDAs are developed. To this end, individual models of FDs (i.e., either Gaussian random spheres or droxtals) were distributed in three-dimensional space with random orientations, reflecting the natural tendency of ice crystals in the atmosphere to have no preferred orientations. Additionally, the following assumptions were made to develop the idealized models of FDAs.

- ~~The shape of all FDs composing a FDA model is identical.~~
- No overlap exists between the constituents of FDA models.
- The maximum number of contact points between the constituents of an FDA model is two.

The aggregation index (*AI*) is used to describe the shape of FDAs in three-dimensional space. The *AI* has been used for analyzing the impacts of three-dimensional shapes of aggregates of ice crystals, such as bullet rosettes and plates, on their corresponding scattering properties (Um and McFarquhar, 2009; Um et al., 2018). The *AI* is defined as

$$AI = \frac{\sum_i^n \sum_j^n D_{ij}}{MAX(\sum_i^n \sum_j^n D_{ij})}, \tag{7}$$

where D_{ij} is the distance between the center of the circumscribing circle of frozen droplet i and that of frozen droplet j. The *AI* is calculated only for the cases where $n \geq 3$ (Um and McFarquhar, 2009; Um et al., 2018). As the *AI* value increases, the shape

of FDAs becomes more similar to that of a linearly-chained structure. A total of ~~270~~ 404 idealized FDAs models were generated, varying the number of constituent FDs (i.e., *n* ranging 2 to 10). Figure 4 shows examples of aggregates of 6 Gaussian random spheres and aggregates of 4 droxtals.

220
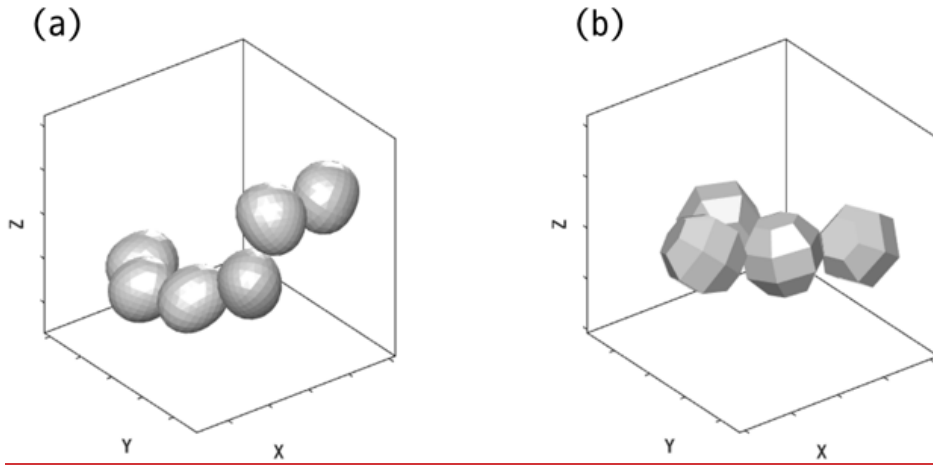
Figure 4. Examples of newly developed models for FDAs. (a) FDAs represented by aggregates of six Gaussian random spheres and, (b) FDAs represented by aggregates of four droxtals.

225 3 Geometric optic method for calculating single-scattering properties

The P_{11} and *g* are single-scattering properties of great interest in both remote sensing and climate models studies. The P_{11} is the first element of the phase matrix (P) that describes the scattering intensity of radiation when the incident light is unpolarized. (Bohren and Huffman, 1983). The *g*, which is defined as the cosine-weighted normalized P_{11}, provides a measure for assessing asymmetry in the forward scattering region of the phase function. The *g* takes on values between -1 and 1 depending on the

230 direction of scattered energy. The *g* equals 1 when all radiation is scattered into the forward hemisphere, and -1 when all radiation is scattered in the backward hemisphere. When *g* equals 0, this indicates isotropic or hemispherically symmetric scattering. The normalized P_{11} and *g* are defined as

$$P_{11} = \frac{1}{4\pi} \int_{4\pi} P_{11} \, d\Omega, \tag{8}$$

$$g = \frac{1}{4\pi} \int_{4\pi} P_{11} \cos\theta d\Omega, \tag{9}$$

235 where Ω and θ is the solid angle and scattering angle, respectively (Bohren and Huffman, 1983).

The geometric optics method (GOM), also known as ray optics or the ray-tracing method, is a widely used approximation technique that calculates single-scattering properties (e.g., P_{11} and *g*) of atmospheric ice crystals (e.g., Yang and Liou, 1995; Macke et al., 1996; Konoshonkin et al., 2015). Furthermore, various methods derived from the GOM, such as improved geometric optics methods (IGOM, Yang and Liou, 1998; Havemann et al., 2002), ray tracing with diffraction on facets (RTDF,

240 Hesse et al., 2008, 2009), and geometrical-optics-integral-equation (GOIE, Ishimoto et al., 2012) have been developed and are in use. The GOM is applicable when the size parameter ($\chi = \frac{2\pi r}{\lambda}$) of scatterers is significantly larger than the wavelength (λ) of incident light (i.e., $\chi \gg 1$), but the lower size limit of the applicability of conventional GOM is not well-defined, and it depends on the morphology of scatterer (Um and McFarquhar, 2015). For the calculation of single-scattering properties of FDs and FDAs, the modified version of the geometric ray-tracing code (Macke et al., 1996), which includes parallelized

245 computation, was used (Um and McFarquhar, 2009).

For the simulations presented here, 72,000 randomly chosen orientations and 1,000 incoming rays per orientation were used to calculate single-scattering properties at $\lambda = 0.80$ μm. The refractive index of ice at this λ is $1.3049 + i1.34\times10^{-7}$ (Warren and Brandt, 2008), where i is the imaginary part, and a scattering angle resolution of 0.25° was employed. The results of simulations are compared with the single-scattering properties measured by a PN during CIRCLE−2 to determine the best-fit model that most accurately matches the observations. To this end, two criteria were used to select the best-fit model: Root Mean Square Error (RMSE) and number of angles (ω) falling within the ± 20% uncertainty range of PN. Essentially, the best-fit model is the one that minimizes RMSE while maximizing ω. The models were sorted by their RMSE values in ascending order, and the model with the largest ω value was selected. In this study, RMSE is defined as ~~The best-fit model minimizing the root mean square error (RMSE), X_{RMSE}, was determined as best-fit model. X_{RMSE} is defined as~~

$$\sim\!\!\!\sim\!\!X_{RMSE}\sim\!\!\!\sim\text{RMSE} = \sqrt{\frac{1}{N}\left\{\sum_{i=1}^{i=32} X_i^2\right\}},$$

(10)

where X_i represents the log difference between the measured average P_{11} and computed P_{11}. The i ($i = 1, 2, …, 32$) is the number of scattering angles measured by the PN instrument.

4 Calculation results and comparison with in situ measurements

The PN, as detailed by Gayet et al. (1997), is an airborne instrument designed to measure the angular scattering pattern, or scattering phase function, of an ensemble of cloud particles ranging from a few micrometers to about 1 mm in diameter. Operating at a wavelength of 0.8 μm, the PN captures scattering angles between ±15° and ±162° with a resolution of 3.5°, typically providing data at 32 distinct angles from among 56 photodiodes (Jourdan et al., 2010). Measurements at near-forward and backward angles ($\theta < 15°$ and $\theta > 162°$) are less reliable due to diffraction effects caused by the edges of holes drilled in the paraboloidal mirror (Gayet et al., 1997). To ensure continuous sampling, the PN integrates the signals from each photodiode over periods selectable by the operator, commonly around 100 ms. The average measurement errors for the angular scattering coefficients range from 3% to 5% for angles between 15° and 162°, with a maximum error reaching 20% at the outermost angles (Shcherbakov et al., 2006). The instrument's ability to directly measure the scattering phase function allows for differentiation of particle types and calculation of essential optical parameters, such as the extinction coefficient and g. Gayet et al. (2002) reported an uncertainty of 25% for the PN-derived extinction coefficient, while the estimated absolute error for the g ranges from ±0.04 to ±0.05, depending on the prevalence of large ice crystals within the cloud (Jourdan et al., 2010).

To determine the ice crystal model that best matches the P_{11} and g of FDAs observed by the PN during CIRCLE−2, the single-scattering properties of individual crystals (i.e., either Gaussian random spheres or droxtals) with varying shapes and those of their aggregates (i.e., either aggregates of Gaussian random spheres or aggregates of droxtals) with varying 3D morphologies (e.g., *AI*) were calculated. Initially, the single-scattering properties of the individual component ice crystals were calculated and then compared with the PN measurements in Section 4.1. A total of 120 Gaussian random spheres (discussed in Sect. 4.1.1) and 129 droxtals (discussed in Sect. 4.1.2) were used for this purpose. This step is crucial to verify whether a constituent crystal can represent the single-scattering properties of their aggregates, as previous studies (Um and McFarquhar, 2007; 2009) have demonstrated similarities between the single-scattering properties of aggregate crystals and their component crystals. Subsequently, the calculated single-scattering properties of homogeneous component aggregates (i.e., either aggregates of Gaussian random spheres ~~(Sect. 4.2.1)~~ or aggregates of droxtals ~~(Sect. 4.2.2)~~) were compared with those observed by the PN (Sect. 4.2 and Supplement). Finally, models for heterogeneous component aggregates, which are mixtures of Gaussian random spheres and droxtals, were developed in Section 4.3.

4.1 Single frozen droplets

4.1.1 Gaussian random sphere

Figure 5a illustrates the comparison between the P_{11} of 120 single FDs models, represented by Gaussian random spheres, and the PN measured average P_{11} reported in previous studies (Baran et al., 2012; Gayet et al., 2012)~~data~~ obtained in the developed overshooting convective cell at 11,080m altitude ($T=-58$ °C) at 13:08:15–13:08:40 UTC on 26 May, 2007 during CIRCLE−2 (i.e., ~~gray shading area~~black filled circles). The P_{11} was divided into three different scattering regions: forward scattering (0° to 60°), lateral scattering (60° to 120°), and backward scattering (120° to 180°) angles, to analyze the relative contribution to each region. Single models of Gaussian random spheres showed average differences of 10.63 $\pm$ 5.19%, 47.28 $\pm$ 27.67%, and 32.19 $\pm$ 12.21% in the forward, lateral, and backward scattering regions, respectively compared with the PN measurements. In particular, the energy scattered into the lateral and backward directions exhibited notable differences compared to that scattered into the forward region. This discrepancy is attributed to the typical characteristic of quasi-spherical ice crystals, low lateral-scattering, as identified by Mishchenko and Travis (1998). Additionally, unlike other non-spherical ice crystals (e.g., hexagonal columns and droxtals), the P_{11} of the Gaussian random sphere did not show sharp peaks in the forward scattering region. The average g was 0.83 ± 0.05 which falls outside the measurement range of the PN (i.e., 0.78 ± 0.04). However, it was shown that the Gaussian random spheres representing spiky forms, as illustrated in case (a), (b), and (c) of Fig. 1, have g values with uncertainty ranges of 0.77 ± 0.04, 0.80 ± 0.04, and 0.81 ± 0.04, respectively, which are close to those of the PN (indicated by blue dashed lines in Fig. 5b). These results, as clearly depicted in Fig. 5b, show that the spherical shape models scatter more intensity into the forward scattering region, consequently leading to an increased g.

To address the discrepancy in the lateral scattering observed in spherical cases of Gaussian random spheres (i.e., (d), (e), and (f) of Fig. 1), additional simulations using the distortion parameter (t) were conducted. Using t is a statistical method reflecting the influence of distorted faces~~, surface roughness, or inclusions~~ of ice crystals on the single-scattering properties. It involves tilting the path of the reflected and refracted ray randomly during the simulation, around its original direction. The zenith and azimuth tilt angles are randomly selected with an equal distribution between 0 and θ_t^{max} and between (0 $\leq \theta_t^{max} \leq$ and 2π, respectively. The degree of distortion is defined by the relation: $t = \theta_t^{max}/90°$ (Macke et al., 1996).

Figure 6 shows box plots analyzing ω, RMSE, and g for single Gaussian random sphere models as a function of t, ranging from 0.0 to 0.95 in 0.05 intervals. The ω slightly increased with t, reaching a maximum of 23 at $t = 0.45$, as it reduced discrepancy in lateral scattering, resulting in more observation angles in the lateral scattering region falling within the PN uncertainty range. However, ω decreases, particularly when t exceeds 0.70, which corresponds to unrealistic, highly distorted surfaces. In contrast to ω, RMSE decreases as t increases, reaching a minimum of 0.0813 at $t = 0.55$, but it also rises when t exceeds 0.70. For g, the average $\pm$ standard deviation of the computed values at $t = 0.65$ was 0.77 ± 0.04, which closely matches the PN measurements (0.78 ± 0.04). However, the smallest difference in g was -0.01% at $t = 0.55$, not at $t = 0.65$. This is because the ω in the forward scattering region at $t = 0.55$ (i.e., 6.39 ± 1.45 out of 12) was greater than at $t = 0.65$ (i.e., 3.91 ± 1.17 out of 12).

Figure 7~~6~~ shows the P_{11} of Gaussian random spheres when assuming varying t values~~:~~ from 0.0 (indicating no distortion)~~, 0.1, 0.2, and 0.3~~ to 0.95 (indicating high distortion). Each ~~black~~ colored solid line (not all lines are shown for brevity) corresponds to the P_{11}, with different values of t, exhibiting the smallest RMSE when compared with the P_{11} measured by the PN (indicated by black filled ~~red~~ circles in Fig. 7~~6~~). A single Gaussian random sphere (i.e., shown in bottom-left side of Fig. 7) with $t = 0.55$~~3~~ was the best-fit model minimizing the RMSE to a value of 0.0813~~1243~~. The differences in the forward, lateral, and backward scattering for the best-fit model were +1.64~~6.89~~%, -0.16~~39.32~~%, and 9.37~~20.16~~%, respectively. The g was calculated to be 0.79~~76~~ which falls within the measurement range of the PN.

The t was applied for the purpose of reducing the difference in the lateral scattering region caused by general features of quasi-spherical ice crystals (i.e., low lateral scattering), and to improve overall agreement with the PN measurements. This

approach effectively minimized the RMSE and increased ω to certain extent (see Fig. 6).~~however, it was not sufficient to minimize the RMSE value.~~ The differences in the P_{11} and g between the Gaussian random sphere models and in situ measurements, across distortion parameter values, are summarized in Table~~s 3 and 4~~ 3.
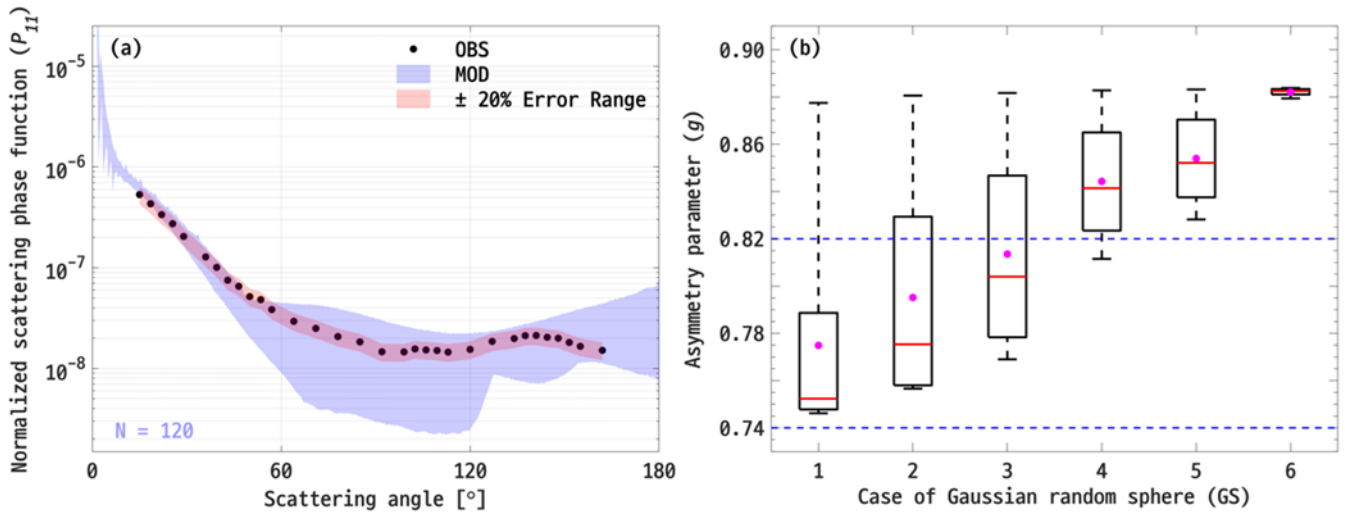
330

Figure 5. (a) A comparison of the computed P_{11} for single Gaussian random sphere models (blue shaded area) against P_{11} obtained during CIRCLE−2 (~~black~~red filled circles). A red shaded area represents the 20% uncertainty range of P_{11} measurements obtained during CIRCLE−2. ~~The gray-shaded area represents the full range of P_{11} measurements of ice crystals obtained during CIRCLE−2.~~ (b) The computed g for each case of individual Gaussian random spheres. The blue dashed lines indicate the uncertainty range for g of PN measurement (i.e., 0.78 ± 0.04). The median and mean ~~values~~ for each case of the single Gaussian random sphere model are plotted as red solid lines and filled magenta circles in the box plot, respectively.

340
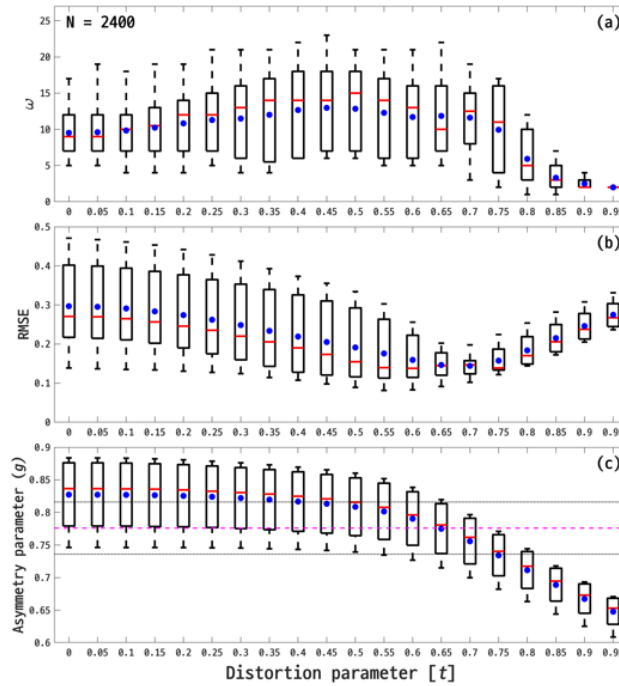
Figure 6. Results for single Gaussian random sphere models with t values ranging from 0.0 to 0.95 in 0.05 intervals, focusing on (a) ω, (b) RMSE, and (c) g. The red solid lines and blue filled circles represent the median and mean, respectively. The black dotted lines and magenta dashed line in panel (c) indicate the boundaries of the PN uncertainty range and the mean of PN measurements (i.e., 0.78 ± 0.04), respectively. The total number of simulated Gaussian random sphere models (N) is shown in the panel (a).

345

Figure 7. A comparison of the average in situ measured P_{11} (represented by black filled circles) with the calculated P_{11} of single Gaussian random sphere models. A red shaded area indicates the ±20% uncertainty range of the PN measurements, and each solid line corresponds to the best-fit model at t values ranging from 0.0 to 0.95 (not all lines are shown here for brevity). The t values for each best-fit line, along with the corresponding ω, RMSE, and g are shown in the upper-right side of the panel. The shape of the single Gaussian random sphere with the minimum RMSE out of 120 models is shown in the bottom-left of the panel.

4.1.2 Droxtals

Figure 87a shows a comparison of the P_{11} of 129 droxtals with the in situ measured P_{11}. Due to their faceted structure, the droxtals have P_{11} characterized by several sharp peaks in the forward scattering directions (Zhang et al., 2004; Um et al., 2011; Yang et al., 2013). The strong peaks are distinctly visible in the P_{11} of droxtals in Fig. 87a and the most pronounced peak was

11

found at 6.5°. These peaks indicate angles of minimal deviation, caused by the refraction of rays passing through two facets of a particle.

For the droxtals, the average differences between the droxtal models and in situ measurements in the forward, lateral, and backward scattering were 4.80 ± 1.90%, 27.06 ± 11.23%, and 15.66 ± 11.09% respectively. The droxtals showed a smaller difference in both the lateral and backward scattering directions compared to ~~that of~~ the Gaussian random sphere. The overall shape of the P_{11} in the forward scattering region appears to deviate significantly from observations. As a result, the average ω in the forward scattering region was 2.00 ± 1.40 out of 12, which is notably smaller than that of Gaussian random sphere (i.e., 5.65 ± 1.19). However, in the lateral and backward scattering regions, ω was 4.51 ± 2.05 out of 11 and 3.99 ± 1.53 out of 9, respectively, indicating that these models effectively simulate the total intensity scattered in the lateral and backward scattering regions compared to the single Gaussian random spheres (i.e., 1.90 ± 1.80 out of 11 and 1.97 ± 1.68 out of 9). With an average RMSE of 0.2462 ± 0.0427 and ω of 10.50 ± 2.85 across four cases, the droxtals demonstrated better performance than the single Gaussian random sphere. ~~However, these models still effectively simulate the total intensity scattered into the region, outperforming the Gaussian random spheres.~~ Figure ~~7~~8b illustrates the comparison of g values of droxtals with the measurement range of the in-situ measurements (indicated by blue dashed lines in Fig. ~~7~~8b) using box plots. Droxtals representing the typical shapes (i.e., (a) in Fig. 3) and the shape most closely resembling columns (i.e., (c) in Fig. 3) have average g of 0.81 ± 0.01 and 0.82 ± 0.01, respectively. These results fall within the upper measurement range of the PN measurements (i.e., 0.78 ± 0.04).

Box plots in Fig. 9 show the analysis of ω, RMSE, and g for single droxtal models with varying t, ranging from 0.0 to 0.95 in 0.05 intervals. Increasing t smooths the forward scattering region of P_{11}, resulting in more observation angles falling within the PN uncertainty range and reducing the differences between the models and PN measurements (see Fig 9a and Table 4). Overall, ω initially rises with t, peaking at 27 when $t = 0.40$ as well as 0.45 and 0.55—higher than for single Gaussian random sphere—and then starts to decrease when t exceeds 0.6. RMSE decreases with t, reaching a minimum value of 0.0637 at $t = 0.5$, but then rises when t exceeds 0.6. At $t = 0.65$, the g had an average of 0.78 ± 0.01, which is a close match to the PN measurements (0.78 ± 0.04).

Figure ~~8~~10 shows the selected P_{11} of droxtals with the smallest RMSE for t ranging from 0.0 to 0.95~~3~~. Each P_{11} of the droxtal is depicted using the colored solid~~black~~ lines, whereas the in situ measurements and their ±20% uncertainty range are represented by ~~red~~ black filled circles and red shaded area, respectively. One distinct finding is the expected disappearance of strong peaks in the forward scattering region as t increases, leading to improved agreement in that region. A single droxtal model using $t = 0.5$ minimized the RMSE to 0.0638 and achieved an ω of 25, both outperforming the single Gaussian random sphere (0.0813 and 17, respectively). The calculated differences between the P_{11} of the droxtal at $t = 0.5$ and the PN measurements were +2.76%, -8.42%, and -9.28% in the forward, lateral, and backward scattering regions, respectively. The g value was found to be 0.80, slightly higher than the average g of PN measurements. A more detailed summary of the statistics for the differences in P_{11} and g between the developed droxtal models and the PN measurements at different t values is provided with Table 4. ~~The P_{11} of droxtals with higher t exhibit smaller difference from the in situ measurements in the lateral and backward scattering region in contrast to the Gaussian random spheres. The disappearance of strong peaks in the forward scattering region, as the t value increases from 0.0 to 0.3, leads to improved agreement in the forward scattering region. Similar to the case with a single Gaussian random sphere, a single droxtal with $t = 0.3$ minimized the RMSE to 0.0806. The calculated differences between the P_{11} of the droxtal with $t = 0.3$ and the in situ measured P_{11} were 2.49%, 3.48%, and 10.64% in the forward, lateral, and backward scattering regions, respectively. The g was found to be 0.81 which is close to the upper boundary of the measurement range of PN. Tables 3 and 4 provide a summary of the average and standard deviation for the differences in the P_{11} and g between developed droxtal models and the in situ measurements at different t values.~~
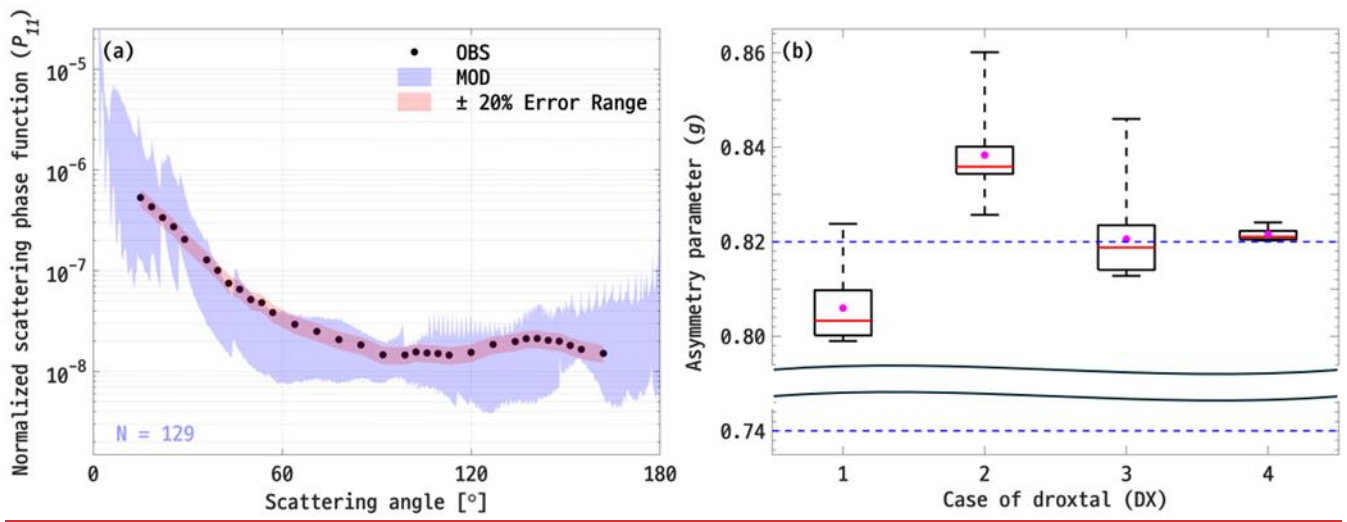
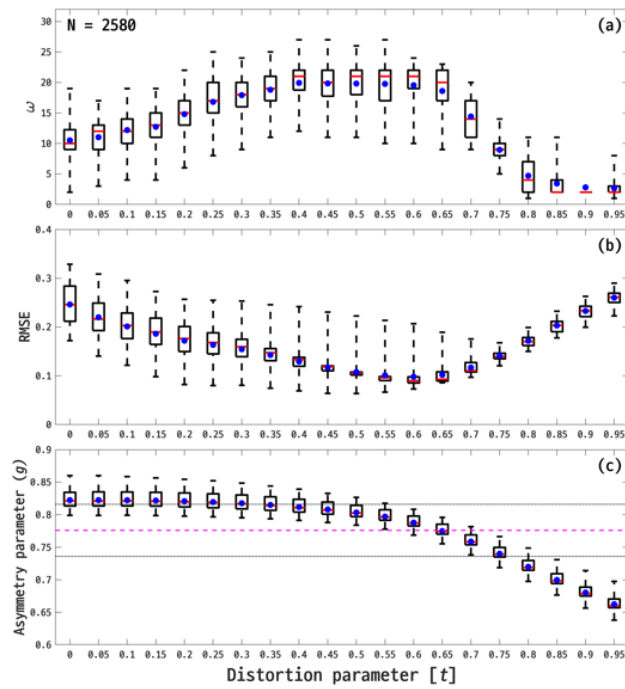**Figure 8. Same as Fig. 5 but for the single droxtal models.**

410

Figure 9. Same as Fig. 6 but for the single droxtal models.
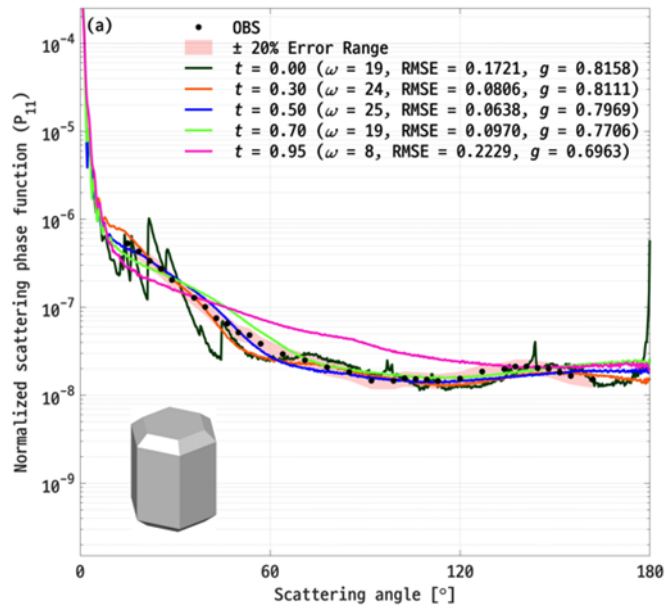
415

13

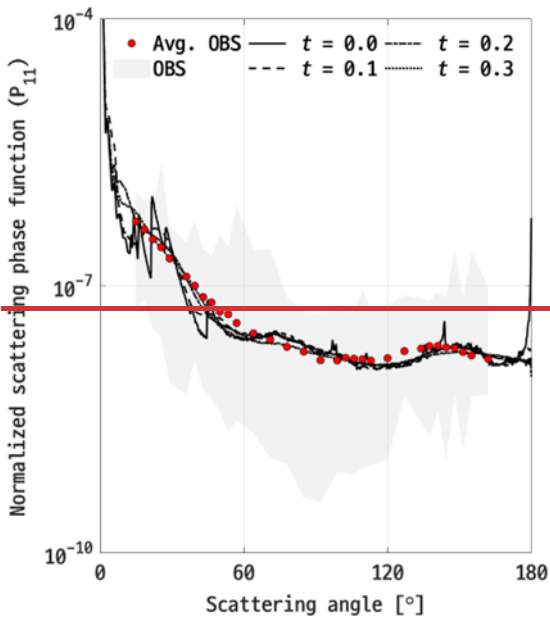**Figure 10. Same as Fig. 7 but for the single droxtal models.**

Figure 8. Same as Fig.6 but for the single droxtal models.

420

425

430 **Table 3. The calculated average ± standard deviation of the difference (relative difference of the best-fit model) in P_{11}, compared to the PN measurements, for 120 single-particle models represented by Gaussian random spheres across the forward (FWD), lateral**

t	FWD	LAT	BWD	*g*	*t*	FWD	LAT	BWD	*g*
0.00	10.63 ± 5.19% (-11.13%)	47.28 ± 27.67% (+69.05%)	32.19 ± 12.21% (+5.91%)	0.83 ± 0.05 (0.76, -2.67%)	0.05	10.62 ± 5.20% (-10.51%)	47.17 ± 27.63% (+67.91%)	32.24 ± 12.24% (+1.65%)	0.83 ± 0.05 (0.75, -2.98%)
0.10	10.58 ± 5.23% (-10.37%)	46.91 ± 27.48 % (+67.31%)	32.41 ± 12.16% (+1.06%)	0.83 ± 0.05 (0.75, -2.99%)	0.15	10.52 ± 5.24% (-10.13%)	46.48 ± 27.16% (+66.21%)	32.59 ± 12.16% (+0.24%)	0.83 ± 0.05 (0.75, -2.99%)
0.20	10.44 ± 5.26% (-9.91%)	45.96 ± 26.73% (+65.35%)	32.78 ± 12.35% (-0.66%)	0.83 ± 0.05 (0.75, -3.05%)	0.25	10.33 ± 5.26% (-9.64%)	45.28 ± 26.13% (+63.98%)	32.88 ± 12.79% (-1.52%)	0.82 ± 0.05 (0.75, -3.13%)
0.30	10.18 ± 5.24% (-6.89%)	44.47 ± 25.42% (+39.32%)	32.85 ± 13.36% (+20.16%)	0.82 ± 0.05 (0.76, -2.60%)	0.35	9.96 ± 5.19% (-6.64%)	43.45 ± 24.70% (+38.58%)	32.67 ± 13.96% (+17.85%)	0.82 ± 0.05 (0.75, -2.74%)
0.40	9.69 ± 5.10% (-6.52%)	42.34 ± 23.90% (+38.24%)	32.31 ± 14.55% (+15.94%)	0.82 ± 0.04 (0.75, -2.96%)	0.45	9.35 ± 4.95% (-3.40%)	41.14 ± 23.08% (+20.95%)	31.66 ± 14.96% (+15.04%)	0.81 ± 0.04 (0.76, -1.88%)
0.50	8.90 ± 4.67% (+2.76%)	39.80 ± 22.14% (−2.72%)	30.42 ± 14.73% (-13.48%)	0.81 ± 0.04 (0.79, +2.15%)	0.55	8.24 ± 4.20% (+1.64%)	38.02 ± 21.16% (-0.16%)	27.96 ± 13.16% (-9.38%)	0.80 ± 0.04 (0.79, +1.21%)
0.60	7.31 ± 3.69% (-0.13%)	35.51 ± 20.36% (+5.00%)	24.15 ± 10.60% (-2.65%)	0.79 ± 0.04 (0.77, -0.15%)	0.65	6.34 ± 3.67% (-0.55%)	32.81 ± 19.98% (+8.56%)	20.18 ± 12.11% (-7.63%)	0.77 ± 0.04 (0.77, -0.36%)
0.70	6.05 ± 4.75% (-0.86%)	31.13 ± 21.90% (+1.59%)	20.01 ± 19.28% (+3.10%)	0.76 ± 0.03 (0.77, -0.97%)	0.75	7.34 ± 6.55% (-2.97%)	32.31 ± 28.29% (+3.71%)	34.34 ± 17.59% (+17.62%)	0.73 ± 0.03 (0.76, -2.60%)
0.80	11.75 ± 6.11% (−5.09%)	40.40 ± 35.22% (+2.07%)	49.77 ± 15.72% (+35.17%)	0.71 ± 0.03 (0.74, -4.11%)	0.85	16.33 ± 5.66% (-10.20%)	58.98 ± 33.51% (+22.35%)	65.22 ± 14.22% (+52.50%)	0.69 ± 0.03 (0.72, -7.49%)
0.90	20.84 ± 5.22% (−15.21%)	76.97 ± 31.57% (+42.63%)	80.42 ± 12.91% (+68.81%)	0.67 ± 0.02 (0.69, -10.67%)	0.95	25.11 ± 4.80% (-19.98%)	93.78 ± 29.39% (+61.84%)	95.22 ± 11.65% (+85.10%)	0.65 ± 0.02 (0.67, -13.56%)

Table 4. Same as Table 3, but for 129 of single droxtal models

t	FWD	LAT	BWD	*g*	*t*	FWD	LAT	BWD	*g*
0.00	4.80 ± 1.90% (-0.01%)	27.06 ± 11.23% (+7.65%)	15.65 ± 11.09% (+1.71%)	0.82 ± 0.01 (0.82, +5.13%)	0.05	4.80 ± 1.96% (-0.02%)	27.02 ± 11.43% (+8.70%)	15.64 ± 10.86% (-1.28%)	0.82 ± 0.01 (0.82, +5.37%)
0.10	4.85 ± 2.02% (-0.01%)	27.07 ± 11.53% (+11.54%)	15.38 ± 11.15% (-7.69%)	0.82 ± 0.01 (0.82, +5.82%)	0.15	4.85 ± 2.10% (-0.06%)	27.03 ± 11.37% (+11.41%)	15.20 ± 11.67% (-8.05%)	0.82 ± 0.01 (0.82, +5.80%)
0.20	4.80 ± 2.10% (+0.03%)	26.75 ± 11.02% (+8.80%)	15.43 ± 11.72% (-4.20%)	0.82 ± 0.01 (0.82, +5.32%)	0.25	5.23 ± 1.79% (+1.23%)	26.85 ± 11.50% (+2.62%)	14.95 ± 11.90% (-7.27%)	0.82 ± 0.01 (0.81, +4.91%)
0.30	5.63 ± 1.56% (+2.49%)	27.05 ± 11.29% (-3.48%)	14.76 ± 12.95% (-10.64%)	0.82 ± 0.01 (0.81, +4.52%)	0.35	5.72 ± 1.44% (+3.06%)	26.61 ± 10.20% (-6.68%)	14.81 ± 13.87% (-11.74%)	0.82 ± 0.01 (0.81, +4.06%)
0.40	5.53 ± 1.36% (+3.25%)	25.16 ± 9.45% (-7.23%)	14.78 ± 14.45% (-13.82%)	0.81 ± 0.01 (0.81, +3.74%)	0.45	5.10 ± 1.27% (+3.14%)	22.92 ± 8.93% (-7.95%)	14.70 ± 14.65% (-12.70%)	0.81 ± 0.01 (0.80, +3.26%)
0.50	4.39 ± 1.19% (+2.76%)	19.57 ± 8.68% (-8.42%)	14.62 ± 14.60% (-9.28%)	0.80 ± 0.01 (0.80, +2.69%)	0.55	3.26 ± 1.11% (+1.95%)	14.87 ± 8.03% (-5.78%)	14.29 ± 14.33% (-7.25%)	0.80 ± 0.01 (0.79, +1.98%)
0.60	1.55 ± 1.00% (+0.66%)	10.47 ± 4.51% (-3.18%)	14.31 ± 12.99% (-0.52%)	0.79 ± 0.01 (0.78, +0.90%)	0.65	1.12 ± 0.94% (-1.78%)	7.43 ± 6.52% (+6.75%)	15.94 ± 11.02% (+5.87%)	0.77 ± 0.01 (0.77, -0.72%)
0.70	4.09 ± 1.15% (-2.48%)	16.08 ± 9.61% (+9.63%)	20.12 ± 11.06% (+3.75%)	0.76 ± 0.01 (0.77, -0.70%)	0.75	7.69 ± 1.25% (-6326%)	31.51 ± 9.59% (+30.94%)	27.26 ± 14.23% (+6.49%)	0.74 ± 0.01 (0.75, -2.77%)
0.80	11.64 ± 1.38% (-10.13%)	48.62 ± 9.37% (+50.10%)	37.12 ± 18.13% (+15.22%)	0.72 ± 0.01 (0.74, -5.22%)	0.85	15.74 ± 1.54% (-13.64%)	66.28 ± 8.96% (+79.40%)	48.87 ± 20.90% (+1.32%)	0.70 ± 0.01 (0.72, -6.59%)
0.90	19.82 ± 1.70% (−16.88%)	83.40 ± 8.50% (+96.31%)	61.39 ± 22.44% (+7.50%)	0.68 ± 0.01 (0.71, -8.54%)	0.95	23.69 ± 1.86% (-19.83%)	99.33 ± 8.01% (+112.04%)	73.97 ± 23.09% (+12.20%)	0.66 ± 0.01 (0.70, -10.27%)

Table 3. Average differences and standard deviations in P_{11} for shape models representing single FDs (either Gaussian random spheres (GS) or droxtals (DX)), across forward (FWD), lateral (LAT), and backward (BWD) scattering regions, with t values ranging from 0.0 to 0.3.

Difference in P_{11} (%)		$t = 0.0$	$t = 0.1$	$t = 0.2$	$t = 0.3$
GS	FWD	10.63 ± 5.19	10.58 ± 5.23	10.44 ± 5.26	10.18 ± 5.24
	LAT	47.28 ± 27.67	46.91 ± 27.48	45.96 ± 26.73	44.47 ± 25.42
	BWD	32.19 ± 12.21	32.41 ± 12.16	32.78 ± 12.35	32.85 ± 13.36
DX	FWD	4.80 ± 1.90	4.85 ± 2.02	4.80 ± 2.10	5.63 ± 1.56
	LAT	27.06 ± 11.23	27.07 ± 11.53	26.74 ± 11.02	27.05 ± 11.29
	BWD	15.65 ± 11.09	15.38 ± 11.15	15.43 ± 11.72	14.76 ± 12.95

440

Table 4. Average differences and standard deviations in g for shape models representing single FDs (either Gaussian random spheres (GS) or droxtals (DX)), across forward (FWD), lateral (LAT), and backward (BWD) scattering regions, with t values ranging from 0.0 to 0.3.

445

Difference in g (%)	$t = 0.0$	$t = 0.1$	$t = 0.2$	$t = 0.3$
GS	7.73 ± 4.71	7.70 ± 4.69	7.52 ± 4.57	7.18 ± 4.57
DX	6.01 ± 1.88	5.99 ± 1.86	5.81 ± 1.83	5.40 ± 1.78

4.2 Aggregates of single frozen droplets

Based on the results of the single-particle models discussed in Section 4.1, models of FDAs were constructed using the
450 Gaussian random sphere and droxtal, which provided the smallest RMSE in comparison to the in situ measurements. These
developed FDAs featured homogeneous components, with the component shapes of the FDAs varying and the number of
components in each model ranging from 2 to 10. For each particle count, 158 different FDAs models were generated (e.g.,
creating 158 models for 2-particle aggregates, 15 18 for 3-particle aggregates, etc.). This approach was applied to both the
Gaussian random spheres and droxtals, so that the total number of developed models amounts to 270324.
455 As the observed FDAs have a myriad range of morphologies including "linearly-chained" or "compact" shapes (Gayet et
al., 2012; Stith et al., 2014; Um et al., 2018), diverse 3D morphological characteristics should be considered. The *AI* (discussed
in Sect. 2.3) was introduced for this purpose. Analysis on the *AI* of the constructed FDAs reveals that for models composed of
homogeneous Gaussian random spheres, the *AI* values range from a minimum of 0.5305 to a maximum of 0.94579480, with a
mean value of 0.75678352. For those composed of homogeneous droxtal components, the minimum, maximum, and mean *AI*
460 values are 0.4224, 0.9738, and 0.73217575, respectively.

Previous research (Um and McFarquhar, 2007; 2009) has shown that the single-scattering properties of aggregates are
similar to those of the individual components. In this study, it was also found that the single-scattering properties of FDAs
constructed with homogeneous components did not significantly differ from those of the individual components, indicating
that the impact of aggregation on the single-scattering properties is not significant. Consequently, the comparison results
465 showed similar trends. To avoid redundancy, a more detailed explanation is provided in the Supplement (S1 and S2) .

4.2.1 Aggregates of Gaussian random spheres

Figure 9 shows the P_{11} and g at $\lambda = 0.80$ μm for aggregates of Gaussian random spheres. . The aggregates of Gaussian random spheres showed an average difference of 13.47%, 80.65%, and 11.06% from the in situ measurements in the forward, lateral, and backward scattering regions, respectively. Although these are minimized to 12.41%, 75.93%, and 6.83% with $t = 0.3$, the discrepancies in the lateral scattering angles remain. One distinct feature is that the discrepancies in the lateral scattering direction from in situ measurements evident in the aggregate of Gaussian random sphere models were also observed for individual Gaussian random sphere models (see Fig. 5a and Fig. 6). These discrepancies remain or even become more pronounced due to the interactions among the components of FDAs. Figure 10 shows the variations of differences in the lateral scattering region of the P_{11} from in situ measurements with t from 0.0 to 0.3. As shown in Fig. 10, as more components are included in a single model of FDAs, the difference between the model and observations tends to increase.

Figure 9b shows how the calculated g varies as a function of the number of attached Gaussian random spheres. An increase in the number of components of FDAs corresponds to a decrease in g. This is attributed to the fact that a higher number of chained FDs results in a longer path length for reflected and refracted rays, consequently leading to a decrease in scattered energy in the forward scattering region. Despite being close to the lower boundary of the measurement range of the PN, FDAs composed of 2 or 3 Gaussian random spheres were found to simulate the g values closer to those observed compared to those with more than 4 components.

Figure 11 shows the P_{11} for aggregates of Gaussian random spheres that have the smallest RMSE with t from 0.0 to 0.3 (i.e., black lines in Fig. 11). The best-fit model, found to be composed of four Gaussian random spheres of type 1 (i.e., (a) in Fig. 1), minimized the RMSE value to 0.1338 when applying $t = 0.3$. The differences between the P_{11} of the best-fit model and the in situ measured P_{11} were 10.43%, 67.60%, and 0.27% in the forward, lateral, and backward scattering regions, respectively. The g was 0.75 which is close to the lower boundary of the PN's uncertainty range. While the P_{11} shows rather reasonable agreement with the in situ measurements in the forward scattering region, it does not accurately simulate the lateral and backward scattering regions of the measurements and notably, no broad peaks are evident at a scattering angle of approximately 140°.
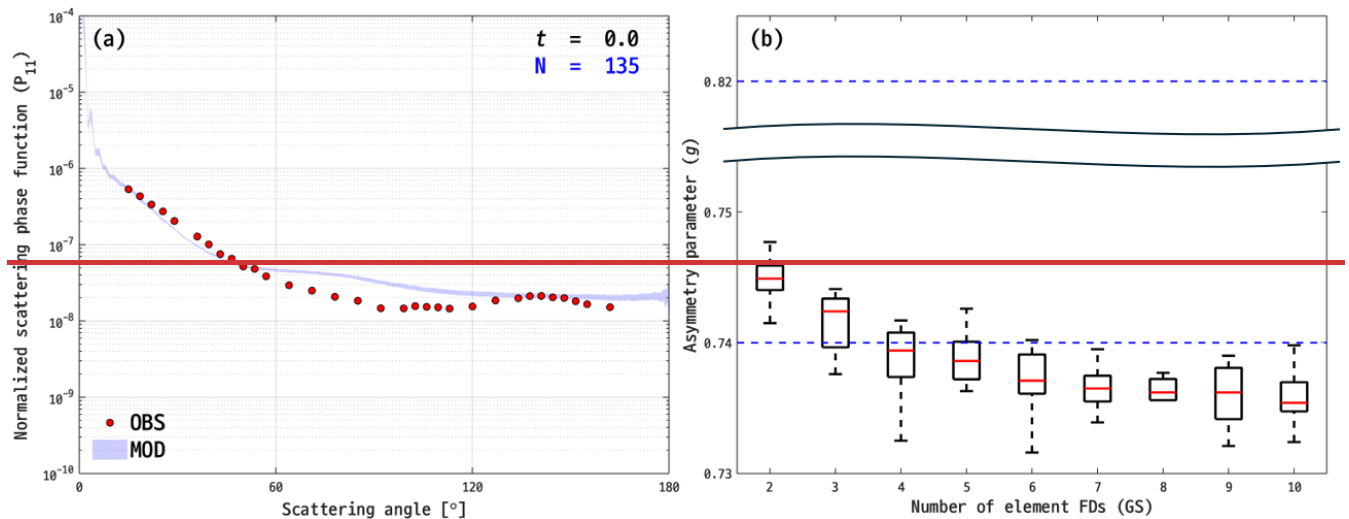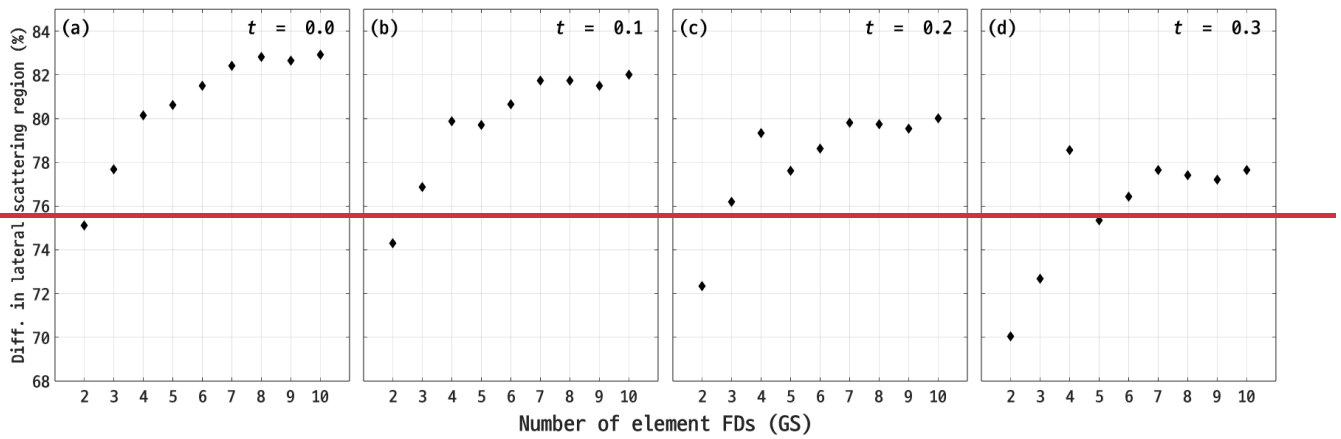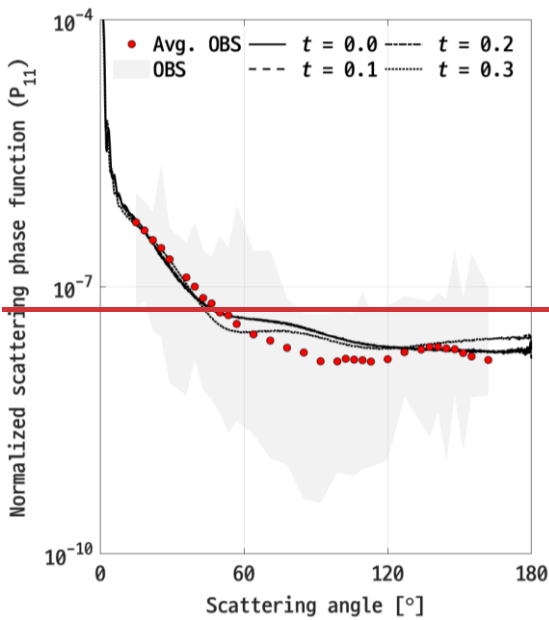

Figure 9. (a) The calculated P_{11} for FDAs represented by aggregates of Gaussian random spheres with distortion parameter $t = 0.0$ at $\lambda = 0.80$ μm. The gray-shaded area and red filled circles represent the full range of P_{11} measurements obtained during CIRCLE-2, respectively. The blue-shaded area indicates the computed P_{11} for FDAs and N denotes the total number of aggregates of Gaussian random spheres developed in this study. (b) The variation in computed g values as a function of the number of components. The red solid line and blue dashed lines represent the median g value for each component count and uncertainty range for the g measured by PN, respectively.

17

18

the *g* values as the number of attached components increases (see Fig. 9b). The average differences from the in situ measurements and standard deviations for both P_{11} and *g* of droxtal aggregates, ranging from no distortion (*t* = 0.0) to *t* = 0.3, are summarized in Tables 5 and 6.

525   Figure 13 shows that the difference from in-situ measurements in lateral scattering for FDAs models represented by droxtals increases with the number of components. However, this difference slightly decreases as the *t* increases from 0.0 to 0.3. In Figure 14, each black line corresponds to the calculated P_{11} for aggregates of droxtals which provide best fit to the measured P_{11} with *t* ranging from 0.0 to 0.3. The best-fit model consisted of two droxtals of type 3 (i.e., (c) of Fig. 3), which gave a minimum RMSE of 0.0550 with *t* = 0.3. The average differences of the best-fit model from in situ measurements were 1.19%,
530   12.43%, and 1.41% in the forward, lateral, and the backward scattering regions, respectively.

        The best-fit model, consisting of aggregates of droxtals, significantly improves agreement with in situ measurements in the lateral scattering region, reducing the difference down to 12.43%. It closely simulates the measurements not only in the lateral scattering region but also in the backward regions, particularly capturing peaks around a 140° scattering angle. The computed *g* for the best-fit model was 0.79 which falls within the measurement range of PN. Tables 5 and 6 summarize the average
535   differences and standard deviations in P_{11} and *g* values between droxtal aggregates and in situ measurements, across *t* values ranging from 0.0 to 0.3.
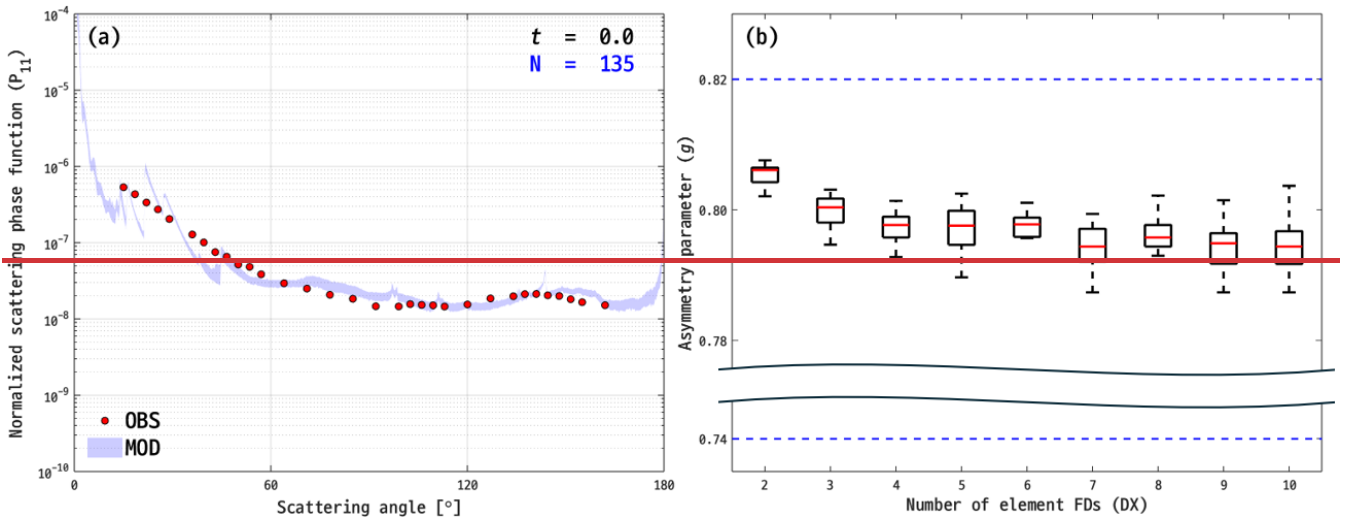
540   Figure 12. Same as Fig. 9 but for the models of FDAs represented by aggregates of droxtals.
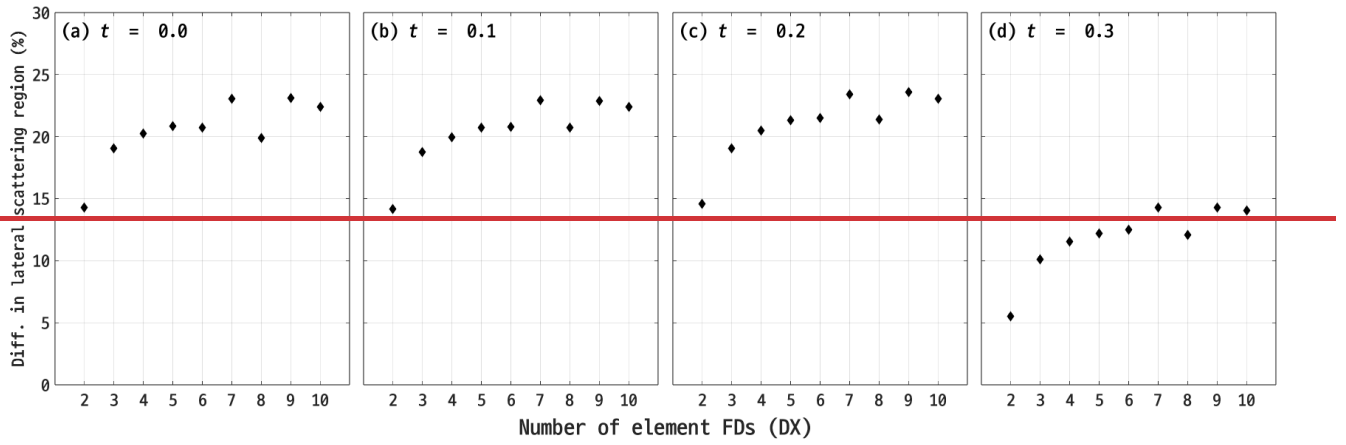
545

19

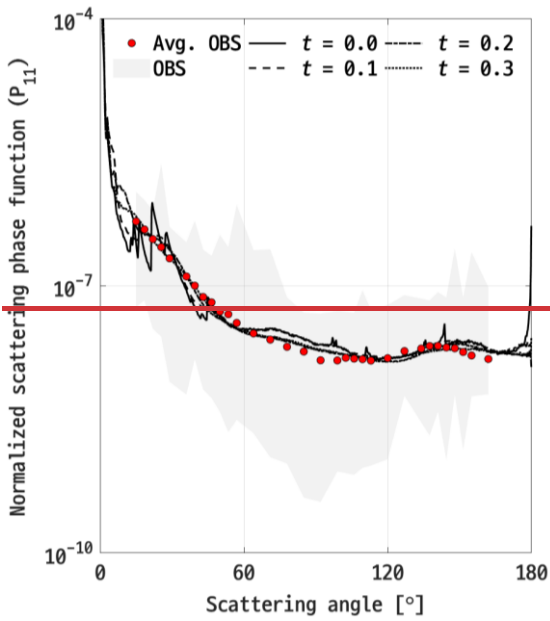Figure 13. Same as Fig. 10 but for the models of FDAs represented by aggregates of droxtals.

Figure 14. Same as Fig.11 but for the FDAs represented by aggregates of droxtals.

Table 5. Same as Table 3 but for the FDAs models represented by aggregates of Gaussian random spheres (FDA_GS) or aggregates of droxtals (FDA_DX).

Difference in P_{11} (%)		$t = 0.0$	$t = 0.1$	$t = 0.2$	$t = 0.3$
	FWD	13.47 ± 0.74	13.28 ± 0.73	12.90 ± 0.72	12.40 ± 0.77
FDA_GS	LAT	80.65 ± 3.16	79.83 ± 3.13	78.14 ± 3.07	75.89 ± 3.31
	BWD	11.06 ± 2.65	10.35 ± 2.63	8.91 ± 2.57	6.81 ± 2.82
	FWD	3.07 ± 0.92	3.10 ± 0.91	3.22 ± 0.88	1.02 ± 0.71
FDA_DX	LAT	20.39 ± 4.20	20.36 ± 4.12	20.93 ± 3.95	11.84 ± 3.93
	BWD	11.27 ± 2.80	10.91 ± 2.81	8.97 ± 2.76	3.33 ± 2.17

20

4.3 Habit mixture model

Different morphological features of FDAs were reported by Stith et al. (2014), with the FDAs comprising of mixtures of quasi-spherical FDs and faceted ice crystals (see Fig. 14 in Stith et al. (2014)). The faceted ice crystals within these aggregates often manifested as hexagonal plates or column crystals. However, the CPI instrument used for capturing images of ice crystals is limited in its ability to fully describe the three-dimensional structures of ice crystals. When imaged by the CPI, ice crystals are presented at specific angles, suggesting that what were identified as hexagonal plates in FDAs may actually be hexagonal facets of droxtals. This interpretation is supported by the experimental findings of Yamazaki and Gonda (1984) and Pedernera and Ávila (2018), which showed that FDs can evolve into hexagonal column-like structures over time.

In previous research, habit mixture models were used to interpret the single-scattering properties of FDAs observed in DCCs during CIRCLE−2. However, the computations of these properties were made indirectly through the weighted habit mixture model (Baran et al., 2012). Baran et al. (2012) introduced four different shape models: Chebyshev particles, spheroids (e.g., prolate and oblate), ice spheres, and highly randomized ten-element hexagonal column aggregates. In the paper, weighting applied to each P_{11} of these models and the sum of weighting equals to one. A combination of two different types of Chebyshev particles and a highly irregular ten-element column aggregate with $t = 0.8$, called model 4 in the paper, provided the best fit to the in situ measurements obtained during CIRCLE−2 (see Fig. 8 of Baran et al., 2012).

In this study, the theoretical method from the previous work is advanced by implementing a direct computation ~~approach. This approach used~~ using habit mixture models~~.,~~ First, the three models with the lowest RMSE and the three models with the highest ω, for both individual Gaussian random spheres and droxtals, as determined in Section 4.1, were selected. This resulted in a total of 12 different individual models, which were then randomly combined to develop the habit mixture models.~~constructed by rearranging components of Gaussian random sphere aggregates and droxtal aggregates.~~ These habit mixture models were developed by varying their 3D morphologies (i.e., *AI*) as discussed in Sect. 2.3. The *AI* values range from a minimum of 0.4808 to a maximum of 0.9787, with a mean value of 0.7540. ~~These aggregates models were found to minimize the RMSE in comparison with in-situ measurements, as detailed in Sect. 4.2.~~ The single-scattering properties of both the habit mixture models developed in this study and the weighted habit mixture models from previous work were computed under conditions identical to those used for the FDs and FDAs models.

Figures 11a, 11b, and 11c present the shapes and P_{11} of three best-matching models (represented by blue solid lines) selected from 80 different habit mixtures developed in this study. A total of 1,120 simulations were conducted using these habit mixture models, and the models that best match the PN measurements are shown. The corresponding t, ω, RMSE, and g with relative difference are provided at the bottom of each panel. The average and ±20% uncertainty range of the PN measurements (represented by black filled circles and red shaded area, respectively) are also shown, along with model 4 (red dashed lines) developed by Baran et al. (2012), denoted as AB12. It should be noted that AB12 was normalized to the PN measurements using the same method as the other models for this comparison.

The first habit mixture model (i.e., Fig. 11a), hereafter referred to as model A, consists of 1 Gaussian random sphere and 3 droxtals. For the P_{11} of model A, when compared to the PN measurements the scattered energy in the forward, lateral, and backward scattering regions differed by +1.03%, +1.69%, and +0.12%, respectively. Model A simulated the energy scattered

21

into the backward scattering region with high accuracy. It led to ω of 29 out of 32 observation angles falling within the PN's uncertainty range, comprising 12 out of 12 in the forward, 10 out of 11 in the lateral, and 7 out of 9 in the backward scattering regions, respectively. The RMSE was minimized to 0.0596 with $t = 0.45$ and g was 0.7852, which is slightly higher than the average of PN measurements.

Figure 11b shows model B, which is a mixture of 3 Gaussian random spheres and 4 droxtals, and the corresponding P_{11}. Compared to model A, model B with $t = 0.40$, exhibited a smaller RMSE of 0.0578 but a slightly decreased ω of 27. Although model B reduced the relative difference in the forward scattering region to -0.18%, the differences in the lateral and backward scattering regions increased to +6.40% and -0.69%, respectively. Consequently, this led to a couple of angles falling outside the PN uncertainty range compared to model A. The increased differences in both the lateral and backward scattering regions, caused by the increase in component number from 4 to 7, allowed for multiple scattering events between the components, leading to more light being scattered in the lateral and backward scattering region, which induces greater discrepancy in those regions.

Next, model C, comprises 1 Gaussian random sphere and 5 droxtals, is depicted in Fig. 11c, which shows its shape and P_{11}. Model C had a smaller RMSE value of 0.0574 compared to the previous two models, with t value of 0.40. The relative differences from the PN measurements in the forward, lateral, and backward scattering regions were -0.44%, +7.08%, and +1.78%, respectively. This result is comparable to model B, despite the difference in the number and fraction of their components. The g was calculated to be 0.7825, which was similar to the previous two models but showed a reduced difference to some extent. Despite the increased relative differences in three different scattering regions and one less ω (i.e., 26 out of 32), when model C compared to model B, RMSE was slightly decreased. To investigate this, the differences in scattered energy were analyzed at specific discrete observation angles, which were divided into three different scattering regions. The average differences at discrete observation angles in the forward, lateral, and backward scattering regions for model C were 8.61 ± 6.78%, 13.01 ± 7.18%, and 12.94 ± 9.75%, respectively. For model B, these were 8.34 ± 6.43%, 13.16 ± 7.66%, and 13.56 ± 8.47%. Model C showed smaller average differences in the lateral and backward scattering regions, which is reflected in its lower RMSE. This comparison supports the above result, as the RMSE was calculated across the 32 observation angles common to both the in situ measurements and the model (see Eq. 10 in Sect. 3).

To reduce the difference in lateral scattering region, model C, which exhibited smallest RMSE, was intentionally modified and additional simulations were conducted. A component represented by a Gaussian random sphere in model C was replaced with a more spherically shaped one. The shape and the P_{11} of modified model C, hereafter referred to as model D, are shown in Fig. 11d. Model D, with +1.30% difference, demonstrated better performance in simulating lateral scattering than models A, B, and C as intended. Although the differences in the forward and backward scattering regions were +1.30% and -5.33%, which were comparable to the others, respectively, the RMSE was minimized to 0.0427 at $t = 0.3$, which is an improved result. The ω was 31 out of 32, with only one angle in the lateral scattering region falling outside the PN uncertainty range. As for g, the replaced spherical component in model D caused a slight increase in scattered energy in the forward scattering region, which led to a deviation from the average g of PN measurements. With g of 0.7985 and a +2.90% relative difference, model D falls within the uncertainty range of PN measurements. Additional simulations were conducted with habit mixture models consisting of different component shapes, however, none performed better than model D.

Next, AB12 was compared to the PN measurements. The relative differences in P_{11} between AB12 and the PN measurements were +2.08%, -9.45%, and -12.09% in the forward, lateral, and backward scattering regions, respectively. As clearly depicted in Fig. 11, there is disagreement in the lateral scattering region. Although AB12 captured the distinct features in the lateral and backward scattering regions, the simulated intensities were much weaker than the observations. These discrepancies in the lateral and backward scattering region led to an RMSE of 0.0663, which is higher than that of model D developed in this study. The ω was 23 out of a total 32 observation angles. For g, it is comparable to the four habit mixture models developed in this study, with a value of 0.79.

Lastly, a weighted habit mixture model (i.e., indirect method) was tested to determine whether similar results to those obtained from model D could be obtained. The P_{11} and g of the components of model D were weighted following the method of Baran et al. (2012). The results showed that directly constructed habit mixture models more accurately simulate the in situ measurements than those developed using the indirect method, as well as single-particle models and aggregates models consisting of homogeneous components. A more detailed explanation is provided in the Supplement (S3).

Figure 15 shows the shapes of three different types of habit mixture models (right most column) developed in this study and the corresponding P_{11} and g of them. The first type of models, henceforth referred to as habit mixture type 1 (HM_T1, see top right panel in Fig. 15), consists of aggregates of Gaussian random spheres and droxtals, each demonstrating the minimum RMSE as discussed in Sections 4.1 and 4.2. The second type, called HM_T2 (see middle right panel in Fig. 15), serves as an alternative version of HM_T1, replacing its components with ones exhibiting maximum sphericity, retaining the same number of components. The third type of habit mixture (HM_T3) as shown in the bottom right panel shares the same shape of Gaussian random spheres as HM_T2, but its droxtal shapes are identical to those in HM_T1. In addition, to investigate the effect of component shape, one Gaussian random sphere was replaced with a droxtal (see bottom right panel in Fig. 15). The 15 different models for each type of habit mixture, or 45 habit mixture models, were generated by varying their 3D morphologies (i.e., *AI*) as discussed in Sect. 2.3. For HM_T1 (HM_T2; HM_T3), the *AI* values range from a minimum of 0.4808 (0.5537; 0.5160) to a maximum of 0.9502 (0.9729; 0.9787), with a mean value of 0.7421 (0.7654; 0.7544).
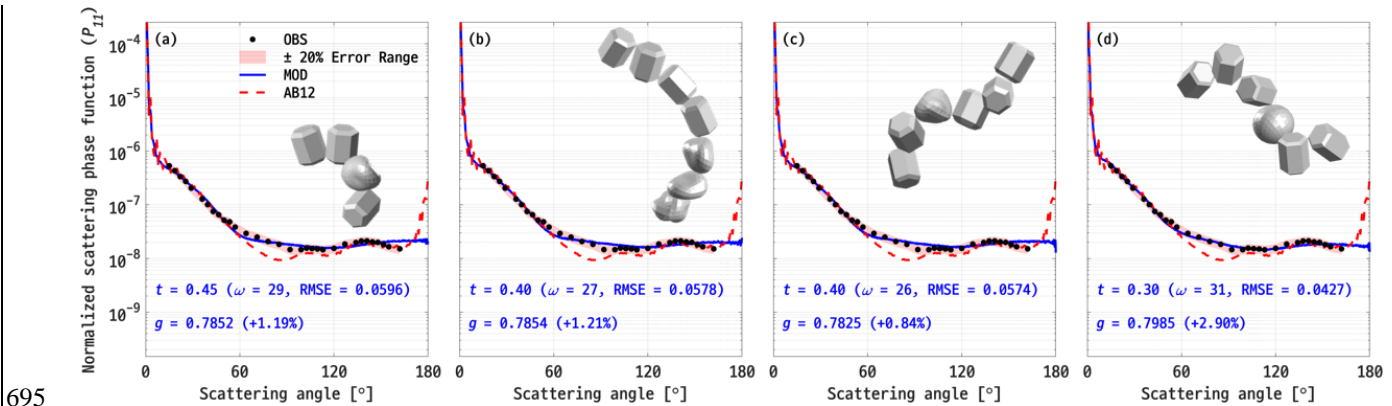
A comparison of the single-scattering properties of the newly developed habit mixture models with the observational data from CIRCLE-2 (i.e., filled red circles in the panels; Gayet et al., 2012) and with model 4 of Baran et al. (2012) (i.e., blue dashed line in the panels) is shown in Fig. 15. The first row of Fig. 15 shows the P_{11} of HM_T1 compared against the in situ measurements. Each column, from left to right, corresponds to $t = 0.0, 0.1, 0.2,$ and 0.3. For the HM_T1, on average, the energy scattered in the forward, lateral, and backward scattering regions for HM_T1 differs by 5.95%, 37.47%, and 9.07% from those of the in situ measurements, respectively. The RMSE was minimized to a value of 0.0713 with $t = 0.3$. The lateral scattering region exhibits slightly improved agreement with the in situ measurements in comparison to the FDAs models which are composed of Gaussian random spheres. However, HM_T1 did not perform as well as those FDA models consisting of homogeneous droxtal components. The HM_T1 models with $t = 0.3$ exhibit high accuracy in simulating the observed g, showing an average value of 0.78.

For HM_T2, the comparison between the computed P_{11} and the in situ measured P_{11} is shown in the second row of Fig. 15. The HM_T2 has its minimum RMSE value of 0.1293 with $t = 0.3$. In the forward, lateral, and backward scattering regions, the average differences between HM_T2 and the in situ measurements were 6.53%, 38.84%, and 4.51%, respectively. Compared to HM_T1, HM_T2 more accurately predicts the peaks in the backward scattering region (138° ~ 141°). However, a higher average difference in the lateral scattering region from in situ measurements than those computed for HM_T1 was present. This difference found in the lateral scattering region is attributed to the Gaussian random spheres which are close to spherical shape. The average computed g for HM_T2 was found to be 0.82, which falls within the upper range of the uncertainty of the PN instrument. This calculated g was higher than that of HM_T1, attributed to greater difference in the forward scattering region of HM_T2. However, in the backward scattering region, specifically between 120° and 150°, HM_T2 demonstrated reasonable agreement.
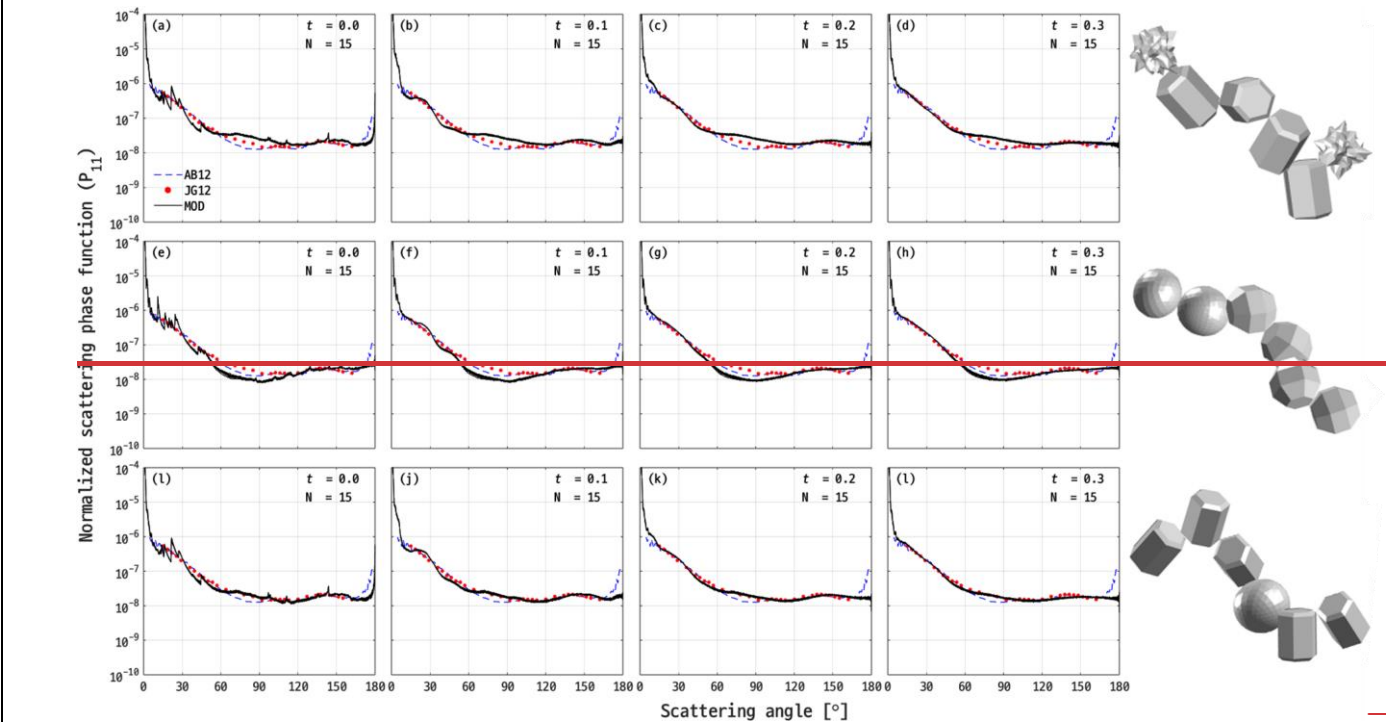
Each panel in the third row of Fig. 15 shows the computed P_{11} of HM_T3. The average differences in the forward, lateral, and backward scattering regions compared to in situ measurements were 1.03%, 2.69%, and 4.33%, respectively. Notably, RMSE for these models minimized to a value of 0.0427 with $t = 0.3$, indicating significant improvement in simulating the in situ measured P_{11}, particularly in the lateral scattering regions compared to other habit mixture models. For example, HM_T3 with $t = 0.3$ shows 0.87%, 0.89%, and 5.37% difference in the forward, lateral, and backward scattering regions, respectively. Moreover, it captures the peak in the back scattering direction more accurately than other habit mixture models. The average

Figure 11. Shapes and P_{11} of the best-fit habit mixture models, along with the corresponding t, ω, RMSE, and g with relative difference. The P_{11} of the weighted habit mixture model developed by Baran et al. (2012) (AB12, red dashed lines), and the PN measurements (black filled circles) with their uncertainty range (red shaded area) are also shown.

5 Summary and Conclusions

In this study, idealized models representing the shapes of FDs and FDAs observed in deep convective clouds were developed based on in situ aircraft measurements and laboratory experiments, and the corresponding single-scattering properties (i.e., scattering-phase function P_{11} and the asymmetry parameter g) were calculated. These computed values of P_{11} and g were subsequently compared with those obtained during the CIRCLE−2 field campaign. Gaussian random spheres and droxtals were proposed as possible candidates for representing the forms of observed FDs and FDAs. A total of 120 individual models of Gaussian random spheres and 129 models of droxtals were generated by varying their shapes. Additionally, by attaching the individual models in both a homogeneous or heterogeneous manner and considering 3D morphologies with varying AI, three different types and a total of ~~315~~ 404 models of FDAs were created as follows: (1) aggregates of Gaussian random spheres; (2) aggregates of droxtals; and (3) mixtures of Gaussian random spheres and droxtals, which are referred to as habit mixtures. ~~The habit mixture models were further categorized into three different types based on variations in shape and component fractions.~~

The P_{11} and g of the newly developed models were calculated using a parallelized version of geometric optics method at λ = 0.80 μm for the comparison with the PN measurements from CIRCLE−2. The distortion parameter (t), an indirect method to represent the distorted faces, ~~surface roughness, or inclusions~~ of natural ice crystals, was also considered in the calculations. The computed P_{11} was divided into three different scattering regions: forward scattering (0° ~ 60°), lateral scattering (60° ~ 120°), and backward scattering (120° ~ 180°), with differences between the calculations and PN measurements analyzed across these regions. The variation in the g from the calculations, ~~and~~ RMSE, and ω compared to the PN measurements were also evaluated. The most important findings of this research are summarized below:

1. For individual models, although the calculated g for both droxtals and Gaussian random spheres falling within the measurement range of the PN, the droxtal exhibited better agreement with the in situ measured P_{11} than the Gaussian random sphere. This finding suggests that faceted ice crystals (e.g., on the droxtal) may be responsible for scattered energy into the lateral scattering region of the observations from CIRCLE−2. However, it may be particularly true for the specific cases from CIRCLE−2. Therefore, it is necessary to carefully examine whether faceted ice crystals are a common occurrence in the upper parts of anvil clouds associated with continental DCCs.

2. The application of the distortion parameter (t) in the calculations of single-scattering properties facilitated the production of smoother P_{11}, reduces g, and increases ω, thereby enhancing the agreement with the PN measurements to certain extent (e.g., up to t = ~0.3). However, beyond this threshold, larger t values diminished the agreement.

3. Constructing FDAs from a heterogeneous mixture of quasi-spherical (i.e., Gaussian random spheres) and faceted crystals (i.e., droxtals) resulted in significantly improved alignment with the PN measurements compared to homogeneous mixtures (i.e., aggregates of solely Gaussian random spheres or droxtals) or individual models (i.e., Gaussian random spheres or droxtals). The heterogeneous mixture model (i.e., model D), which consists of 1 Gaussian random sphere and 5 droxtals, demonstrated the closest match to PN measurements. This model effectively replicated P_{11} and g, minimized the RMSE to 0.0427, and achieved a high level of agreement with an ω value of 31 out of 32.

4. Calculations of single-scattering properties for FDAs using a direct computational approach, in which FDAs were generated by aggregating heterogeneous components, yielded more accurate results compared to the indirect method, where single-scattering properties were computed by weighting the calculated P_{11} of individual shape models. This finding underscores the critical importance of employing realistic shape models and highlights the significant impact of the aggregation process on the calculations of single-scattering properties of aggregate ice crystals.

1. ~~Overall, discrepancies over the scattering angles and the RMSE values were minimized when t = 0.3 was applied to the shape models developed in this study.~~

25

2. For P_{11} of a single droxtal with $t = 0.3$, differences with the in situ measurement were 2.49%, 3.48%, and 10.64% in the forward, lateral, and backward scattering regions, respectively. The RMSE was minimized to a value of 0.0806. The g value was 0.81 which is close to the upper range of uncertainty observed by the PN (0.78 ± 0.04).

3. The Gaussian random sphere with $t = 0.3$ was less effective than the droxtal in simulating the in situ measured P_{11}, with differences of 6.89%, 39.32%, and 20.16% in the forward, lateral, and backward scattering regions, respectively. These differences, especially in the lateral scattering direction, were one of the characteristics for spherical shape models that contributed to a higher RMSE of 0.1243. Nonetheless, the calculated g of 0.76 fell within the measurement range of PN.

4. For individual models, despite the calculated g for both droxtals and Gaussian random spheres falling within the measurement range of the PN, the droxtal exhibits better agreement with the in situ measured P_{11} than the Gaussian random sphere. This finding suggests that faceted ice crystals (e.g., on the droxtal) may be responsible for scattered energy into the lateral scattering region of the observations from CIRCLE-2. However, it may be particularly true for the specific cases from CIRCLE-2. Therefore, it is necessary to carefully examine whether faceted ice crystals are a common occurrence in the upper parts of anvil clouds associated with continental DCCs.

5. For the FDAs with homogeneous components (i.e., either aggregates of Gaussian random spheres or aggregates of droxtals), the aggregates of droxtals with $t = 0.3$ show the minimum RMSE of 0.0549, showing differences from in situ measurements of 1.19%, 12.43%, and 1.41% in the forward, lateral, and backward scattering regions, respectively. The computed g value was found to be 0.79.

6. In contrast, aggregates of Gaussian random spheres with $t = 0.3$ show larger differences of 10.44%, 67.60%, and 0.27% in the forward, lateral, and backward scattering regions, respectively, leading to a higher RMSE value of 0.1338. The calculated g was 0.75.

7. The third type habit mixture (i.e., HM_T3), which is a combination of five droxtals and one Gaussian random sphere, matched the PN measurements most closely. It effectively minimized the differences from in situ measurements to 0.87%, 0.89%, and 5.37% in the forward, lateral, and backward scattering directions, respectively. The RMSE for HM_T3 was reduced to a value of 0.0427, and the corresponding g was 0.80.

8. In the comparison, the difference and RMSE between the weighted habit mixture model developed by Baran et al. (2012) and in situ measurements had larger differences of 2.08%, 9.45%, and 12.09% in the forward, lateral, and backward scattering region, respectively. This resulted in an increased RMSE of 0.0663. The corresponding g was 0.79.

9. The assumption that FDAs consist of homogeneous components was found to be inadequate for interpreting the in situ measured single-scattering properties. Instead, constructing FDAs from a heterogeneous mixture of quasi-spherical (i.e., Gaussian random spheres) and faceted (i.e., droxtal) components showed the best match for the single-scattering properties of FDAs measured in situ.

The findings of this study have significant suggest potential implications for improving the accuracy of simulations regarding the radiative impacts of deep convective clouds and associated anvils on the Earth's climate system. A comprehensive understanding of the single-scattering properties of the constituent particles of deep convective clouds is essential to effectively interpret and represent the role of these clouds in large-scale climate models. To this end, in-situ measurements of single-scattering properties obtained during the field campaign were analyzed using shape models that represent the observed habits, along with methods for calculating these properties. In this research, interpreting in situ measured single-scattering properties using models of aggregates with heterogeneous components has proven to be more accurate than aggregate models with homogeneous components or individual shape models. This result agrees with the interpretations with weighted habit mixture models proposed by Baran et al. (2012). Nonetheless, it is important to note that these conclusions may be particularly relevant to the specific cases analyzed in this study, highlighting the need to investigate whether FDAs with heterogeneous components are a common feature of deep convective clouds (Stith et al., 2014). Furthermore, the in situ measurements used to assess the

developed models did not sufficiently resolve the backward scattering region, which are sensitive to variations in the orientation, shape, and heterogeneities (e.g., distorted surfaces, surface roughness, or inclusions) of ice crystals. In this respect, it should be emphasized that the measurements of the intensities of scattered light across the full range of scattering angles, coupled with images of ice crystals are required. The use of an advanced cloud probe, such as a particle habit imaging and

795 polar scattering probe (Abdelmonem et al., 2016; Schnaiter et al., 2018; Waitz et al., 2021), capable of capturing the detailed 3D morphologies of FDs or FDAs, is essential to further this understanding. Additionally, cloud chamber experiments, where the atmospheric conditions of deep convective clouds can be accurately replicated and studied repeatedly, could offer a viable solution for obtaining more accurate single-scattering measurements or exploring the mechanisms of producing FDAs which is not covered in this study.

800

Code Availability

Code is available from the corresponding author on reasonable request.

Data Availability

All raw data can be provided by the corresponding authors upon reasonable request.

805 **Author Contributions**

JK, JU, and GMM conceived the study. JK and SP ran the model simulations. AJB analyzed and provided CIRCLE−2 PN measurements. JK, SP, JU, JWC, KL, SSL, CHJ, KSL performed the result comparison. JK prepared the manuscript with contributions from all co-authors. All authors were involved in the scientific interpretation and discussion.

Competing Interests

810 One author is a member of the editorial board of Atmospheric Chemistry and Physics

References

Abdelmonem, A., Järvinen, E., Duft, D., Hirst, E., Vogt, S., Leisner, T., and Schnaiter, M.: PHIPS–HALO: the airborne Particle

825 Habit Imaging and Polar Scattering probe – Part 1: Design and operation, Atmos. Meas. Tech., 9, 3131–3144, https://doi.org/10.5194/amt-9-3131-2016, 2016.

Andreae, M. O., Rosenfeld, D., Artaxo, P., Costa, A. A., Frank, G. P., Longo, K. M., and Silva-Dias, M. A.: Smoking rain clouds over the Amazon., Science, 303(5662), 1337–1342, https://doi.org/10.1126/science.1092779, 2004.

Baran, A. J, Francis, P. N., Labonnote, L. C., and Dutriaux-Boucher, M.: A scattering phase function for ice cloud: Tests of applicability using aircraft and satellite multi-angle multi-wavelength radiance measurements of cirrus, Q. J. Roy. Meteorol. Soc., 127, 2395–2416, https://doi.org/10.1002/qj.49712757711, 2001.

Baran, A. J.: The dependence of cirrus infrared radiative properties on ice crystal geometry and shape of the size-distribution function, Q. J. Roy. Meteorol. Soc., 131, 1129–1142, https://doi.org/10.1256/qj.04.9, 2005.

Baran, A. J. and Labonnote, L. C.: A self-consistent scattering model for cirrus. I: the solar region, Q. J. Roy. Meteorol. Soc., 133, 1899–1912, https://doi.org/10.1002/qj.164, 2007.

Baran, A. J.: A review of the light scattering properties of cirrus, J. Quant. Spectrosc. Ra., 110, 1239–1260, https://doi.org/10.1016/j.jqsrt.2009.02.026, 2009.

Baran, A. J., Gayet, J.-F., and Shcherbakov, V.: On the interpretation of an unusual in-situ measured ice crystal scattering phase function, Atmos. Chem. Phys., 12, 9355–9364, https://doi.org/10.5194/acp-12-9355-2012, 2012.

Barth, M. C., Cantrell, C. A., Brune, W. H., Rutledge, S. A., Crawford, J. H., Huntrieser, H., Carey, L. D., MacGorman, D., Weisman, M., Pickering, K. E., Bruning, E., Anderson, B., Apel, E., Biggerstaff, M., Campos, T., Campuzano-Jost, P., Cohen, R., Crounse, J., Day, D. A., Diskin, G., Flocke, F., Fried, A., Garland, C., Heikes, B., Honomichl, S., Hornbrook, R., Huey, L. G., Jimenez, J. L., Lang, T., Lichtenstern, M., Mikoviny, T., Nault, B., O'Sullivan, D., Pan, L. L., Peischl, J., Pollack, I., Richter, D., Riemer, D., Ryerson, T., Schlager, H., St Clair, J., Walega, J., Weibring, P., Weinheimer, A., Wennberg, P., Wisthaler, A., Wooldridge, P. J., and Ziegler, C.: The Deep Convective Clouds and Chemistry (DC3) Field Campaign, Bull. Am. Meteorol. Soc., 96, 1281–1309, https://doi.org/10.1175/BAMS-D-13-00290.1, 2015.

Bohren, C. F. and Huffman, D. R.: Absorption and scattering of light by small particles, Wiley, 530 pp., 1983.

Connolly, P. J., Saunders, C. P. R., Gallagher, M. W., Bower, K. N., Flynn, M. J., Choularton, T. W., Whiteway, J., and Lawson, R. P.: Aircraft observations of the influence of electric fields on the aggregation of ice crystals, Q. J. Roy. Meteorol. Soc., 131, 1695–1712, https://doi.org/10.1256/qj.03.217, 2005.

Crépel, O., Gayet, J. F., Fournol, J. F., and Oshchepkov, S.: A new airborne polar nephelometer for the measurement of optical and microphysical cloud properties. Part II: Preliminary tests, Ann. Geophys., 15, 460–470, https://doi.org/10.1007/s00585-997-0460-0, 1997.

Dauhut, T. and Hohenegger, C.: The contribution of convection to the stratospheric water vapor: The first budget using a global storm-resolving model., J. Geophys. Res. Atmos., 127, e2021JD036295. https://doi.org/10.1029/2021JD036295, 2022.

de Reus, M., Borrmann, S., Bansemer, A., Heymsfield, A. J., Weigel, R., Schiller, C., Mitev, V., Frey, W., Kunkel, D., Kürten, A., Curtius, J., Sitnikov, N. M., Ulanovsky, A., and Ravegnani, F.: Evidence for ice particles in the tropical stratosphere from in-situ measurements, Atmos. Chem. Phys., 9, 6775–6792, https://doi.org/10.5194/acp-9-6775-2009, 2009.

Doswell III, C. A. and Bosart, L. F.: Extratropical synoptic-scale processes and severe convection. Storms, 1, 37–75, 2001.

~~Feng, Z., Dong, X. Q., Xi, B. K., Schumacher, C., Minnis, P., and Khaiyer, M.: Top of atmosphere radiation budget of convective core/stratiform rain and anvil clouds from deep convective systems, J. Geophys. Res. Atmos., 116, D23202, https://doi.org/10.1029/2011JD016451, 2011.~~

Frey, W., Borrmann, S., Kunkel, D., Weigel, R., de Reus, M., Schlager, H., Roiger, A., Voigt, C., Hoor, P., Curtius, J., Krämer, M., Schiller, C., Volk, C. M., Homan, C. D., Fierli, F., Di Donfrancesco, G., Ulanovsky, A., Ravegnani, F., Sitnikov, N. M., Viciani, S., D'Amato, F., Shur, G. N., Belyaev, G. V., Law, K. S., and Cairo, F.: In situ measurements of tropical cloud properties in the West African Monsoon: upper tropospheric ice clouds, Mesoscale Convective System outflow, and subvisual cirrus, Atmos. Chem. Phys., 11, 5569–5590, https://doi.org/10.5194/acp11-5569-2011, 2011.

Gayet, J. F., Crépel, O., Fournol, J. F., and Oshchepkov, S.: A new airborne polar nephelometer for the measurements of optical and microphysical cloud properties. Part I: Theoretical design, Ann. Geophys., 15, 451–459, https://doi.org/10.1007/s00585-997-0451-1, 1997.

Gayet, J. F., Asano, S., Yamazaki, A., Uchiyama, A., Sinyuk, A., Jourdan, O., and Auriol, F.: Two case studies of winter continental-type water and mixed-phase stratocumuli over the sea 1. Microphysical and optical properties, J. Geophys. Res. Atmos., 107, 11-1–11-15, https://doi.org/10.1029/2001JD001106, 2002.

Gayet, J. F., Mioche, G., Bugliaro, L., Protat, A., Minikin, A., Wirth, M., Dornbrack, A., Shcherbakov, V., Mayer, B., Garnier, A., and Gourbeyre, C.: On the observation of unusual high concentration of small chain-like aggregate ice crystals and large ice water contents near the top of a deep convective cloud during the CIRCLE−2 experiment, Atmos. Chem. Phys. 12, 727–744, https://doi.org/10.5194/acp-12-727-2012, 2012.

Hartmann, D. L.: Tropical anvil clouds and climate sensitivity, P. Nat. Acad. Sci. USA, 113, 8897–8899, https://doi.org/10.1073/pnas.161045511, 2016.

Hartmann, D. L. and Berry, S. E.: The balanced radiative effect of tropical anvil clouds, J. Geophys. Res. Atmos., 122, 5003–5020, https://doi.org/10.1002/2017JD026460, 2017.

Havemann, S., Baran, A. J., and Edwards, J. M.: Implementation of the T-matrix method on a massively parallel machine: a comparison of hexagonal ice cylinder single-scattering properties using the T-matrix and improved geometric optics methods, J. Quant. Spectrosc. Ra., 79–80, 707–720, https://doi.org/10.1016/S0022-4073(02)00316-3, 2003.

Hesse, E.: Modelling diffraction during ray tracing using the concept of energy flow lines, J. Quant. Spectrosc. Ra., 109, 1374–1383, https://doi.org/10.1016/j.jqsrt.2007.11.002, 2008.

Hesse, E, Mc Call, D. S., Ulanowski, Z., Stopford, C., and Kaye, P. H.: Application of RTDF to particles with curved surfaces, J. Quant. Spectrosc. Ra., 110, 1599–1603, https://doi.org/10.1016/j.jqsrt.2009.01.011, 2009.

Heymsfield, A. J. and Sabin, R. M.: Cirrus Crystal Nucleation by Homogeneous Freezing of Solution Droplets, J. Atmos. Sci. 46, 2252–2264, https://doi.org/10.1175/1520-0469(1989)046<2252:CCNBHF>2.0.CO;2, 1983.

Houze, R. A.: Orographic effects on precipitating clouds. Reviews of Geophysics, 52(3), 809–879, 2014.

Ishimoto, H., Masuda, K., Mano, Y., Orikasa, N., and Uchiyama, A.: Irregularly shaped ice aggregates in optical modeling of convectively generated ice clouds, J. Quant. Spectrosc. Ra., 113, 632–643, https://doi.org/10.1016/j.jqsrt.2012.01.017, 2012.

Jang, S., Kim, J., McFarquhar, G. M., Park, S., Han, S., Lee. S. S., Jung C. H., Jung, H., Chang, K.-H., Jung, W., and Um, J.: The impacts of single-scattering properties and microphysical properties of ice particles smaller than 100 μm on the bulk radiative properties of tropical cirrus, Remote Sensing, 14, 3002, https://doi.org/ 10.3390/rs14133002, 2022.

Järvinen, E., Schnaiter, M., Mioche, G., Jourdan, O., Shcherbakov, V., Costa, A., Afchine, A., Krämer, M., Heidelberg, F., Jurkat, T., Voigt, C., Schlager, H., Nichman, L., Gallagher, M., Hirst, E., Schmitt, C., Bansemer, A., Heymsfield, A., Lawson, P., Tricoli, U., Pfeilsticker, K., Vochezer, P., Möhler, O., and Leisner, T.: Quasi-Spherical Ice in Convective Clouds, J. Atmos. Sci., 10, 3885–3910, https://doi.org/10.1175/JAS-D-15-0365.1, 2016.

Jensen, E. J., Toon, O. B., Selkirk, H. B., Spinhirne, J. D., and Schoeberl, M. R.: On the formation and persistence of subvisible cirrus clouds near the tropical tropopause, J. Geophys. Res. Atmos., 101, 21361–21375, https://doi.org/10.1029/95JD03575, 1996.

Jourdan, O., Mioche, G., Garret, T. J., Schwarzenbock, A., Vidot, J., Xie, Y., Shcherbakov, V., Duroure, C., Yang, P., and Gayet, J.-F.: Coupling of the microphysical and optical properties of arctic clouds during the ASTAR 2004 experiment: Implications for light scattering modelling, J. Geophys. Res. Atmos., 115, D23206, doi:10.1029/2010JD014016, 2010.

Konoshonkin, A. V., Kustova, N. V., and Borovoi, A., G.: Beam Splitting Algorithm for the Problem of Light Scattering by Atmospheric Ice Crystals. Part 1. Theoretical Foundations of the Algorithm, Atmos. Ocean. Opt., 28, 441–447, https://doi.org/10.1134/S1024856015050097, 2015.

Lawson, R. P., Baker, B. A., and Pilson, B. L.: In-Situ measurements of microphysical properties of mid-latitude and anvil cirrus, Proceedings, 30th International Symposium on Remote Sensing of Environment, November, Honolulu, Hawaii, 707–710, 2003.

915 Lawson, R. P., Jensen, E., Mitchell, D. L., Baker, B., Mo, Q., and Pilson, B.: Microphysical and radiative properties of tropical clouds investigated in TC4 and NAMMA, J. Geophys. Res. Atmos., 115, D00J08, https://doi.org/10.1029/2009JD013017, 2010.

Lee, S. S., Jung, C. H., C. H. Jung, Chiao, S., S. Chiao, Um, J., J. Um, Choi, Y. S., Y. S. Choi, and Choi, W. J. W. J. Choi, 2019: Comparison of simulations of updraft mass fluxes and their response to increasing aerosol concentration between a bin 920 scheme and a bulk scheme in a deep-convective cloud system., Advances in Meteorology, vol. 2019, Article ID 9292535, 29 pages, https://doi.org/10.1155/2019/9292535, 2019.

Macke, A.: Scattering of Light by Polyhedral Ice Crystals, Appl. Opt., 32, 2780-2788, https://doi.org/10.1364/AO.32.002780, 1993.

Macke, A., Mueller, J., and Raschke, E.: Single scattering properties of atmospheric ice crystals, J. Atmos. Sci., 53, 2813– 925 2825, https://doi.org/10.1175/1520-0469(1996)053<2813:SSPOAI>2.0.CO;2, 1996.

Magee, N. B., Boaggio, K., Staskiewicz, S., Lynn, A., Zhao, X. Y., Tusay, N., Schuh, T., Bandamede, M., Bancroft, L., Connelly, D., Hurler, K., Miner, B., and Khoudary, E.: Captured cirrus ice particles in high definition, Atmos. Chem. Phys., 21, 7171–7185, https://doi.org/10.5194/acp-21-7171-2021, 2021.

McFarquhar, G. M., Yang, P., Macke, A., and Baran, A. J.: A new parameterization of single scattering solar radiative 930 properties for tropical anvils using observed ice crystal size and shape distributions, J. Atmos. Sci., 59, 2458–2478, https://doi.org/10.1175/1520-0469(2002)059<2458:ANPOSS>2.0.CO;2, 2002.

Mishchenko, M. I. and Travis, L. D.: Capabilities and limitations of a current FORTRAN implementation of the T-matrix method for randomly oriented rotationally symmetric scatterers, J. Quant. Spectrosc. Ra., 60, 309–324, https://doi.org/10.1016/S0022-4073(98)00008-9, 1998.

935 Mugnai, A. and Wiscombe, W. J.: Scattering of radiation by moderately nonspherical particles, J. Atmos. Sci., 37, 1291–1307, https://doi.org/10.1175/1520-0469(1980)037<1291:SORBMN>2.0.CO;2, 1980.

Muinonen, K., Nousiainen, T., Fast, P., Lumme, K., and Peltoniemi, J. I.: Light scattering by Gaussian random particles: Ray optics approximation, J. Quant. Spectrosc. Ra., 55, 577–601, https://doi.org/10.1016/0022-4073(96)00003-9, 1996.

Muinonen, K. and Lagerros, J. S. V.: Inversion of shape statistics for small solar system bodies, Astron. Astrophys., 333, 753– 940 761, 1998.

Muinonen, K., Zubko, E., Tyynela, J., Shkuratov, Y. G., and Videen, G.: Light scattering by Gaussian random particles with discrete-dipole approximation, J. Quant. Spectrosc. Ra., 106, 360–377, https://doi.org/10.1016/j.jqsrt.2007.01.049, 2007.

Nairy, C. M.: Observations of Chain Aggregates in Florida Cirrus Cloud Anvils On 3 August 2019 During CAPEEX19, M.S. thesis, University of North Dakota, USA, 105 pp., 2022.

945 Nousiainen, T.: Light scattering by nonspherical atmospheric particles, Ph.D. thesis, University of Helsinki, Finland, 53 pp., 2002.

Nousiainen, T., Muinonen, K., and Raisanen, P.: Scattering of light by large Saharan dust particles in a modified ray optics approximation, J. Geophys. Res. Atmos., 108(D1), 4025, https://doi.org/10.1029/2001JD001277, 2003.

Nousiainen, T. and McFarquhar, G. M.: Light Scattering by Quasi-Spherical Ice Crystals, J. Atmos. Sci., 61, 2229–2248, 950 https://doi.org/10.1175/1520-0469(2004)061<2229:LSBQIC>2.0.CO;2, 2004.

Nousiainen, T., Lindqvist, H., McFarquhar, G. M., and Um, J.: Small irregular ice crystals in tropical cirrus, J. Atmos. Sci., 68, 2614–2627, https://doi.org/10.1175/2011JAS3733.1, 2011.

Ohtake, T.: Unusual Crystals in Ice Fog, J. Atmos. Sci., 27, 509–511, https://doi.org/10.1175/1520-0469(1970)027<0509:UCIIF>2.0.CO;2, 1970.

955 Pedernera, D. A. and Ávila, E. E.: Frozen-droplets aggregation at temperature below −40 ∘C, J. Geophys. Res. Atmos., 123, 1244–1252, 2018.

Phillips, V. T. J., Donner, L. J., and Garner, S. T.: Nucleation processes in deep convection simulated by a cloud-system-resolving model with double-moment bulk microphysics, J. Atmos. Sci., 64, 738–761, https://doi.org/10.1175/JAS3869.1, 2007.

960 Raymond, D. J. and Blyth, A. M.: The role of convective clouds in the Earth's energy balance. Earth's Future, 4(11), 537–542, 2016.

Rosenfeld, D. and Woodley, W. L.: Deep convective clouds with sustained supercooled liquid water down to -37.5℃, Nature, 405, 440–442, https://doi.org/10.1038/35013030, 2000.

Saunders, C. P. R. and Wahab, N. M. A.: The influence of electric fields on the aggregation of ice crystals, J. Meteorol. Soc. 965 Jpn., 53, 121–126, 1975.

Schnaiter, M., Järvinen, E., Abdelmonem, A., and Leisner, T.: PHIPS-HALO: the airborne particle habit imaging and polar scattering probe–Part 2: Characterization and first results, Atmos. Meas. Tech., 11, 341-357, https://doi.org/10.5194/amt-11-341-2018, 2018.

Shcherbakov, V., Gayet, J. F., Baker, B., and Lawson, P.: Light scattering by single natural ice crystals, J. Atmos. Sci., 63, 970 1513–1525, https://doi.org/10.1175/JAS3690.1, 2006.

Stith, J. L., Dye, J. E., Bansemer, A., Heymsfield, A. J., Grainger, C. A., Petersen, W. A., and Cifelli, R.: Microphysical observations of tropical clouds, J. Appl. Meteorol. Clim., 41, 97–117, https://doi.org/10.1175/1520-0450(2002)041%3C0097:MOOTC%3E2.0.CO;2, 2002.

975 Stith, J. L., Haggerty, J. A., Heymsfield, A. J., and Grainger, C. A.: Microphysical Characteristics of Tropical Updrafts in Clean Conditions, J. Appl. Meteorol. Clim., 43, 779–794, https://doi.org/10.1175/2104.1, 2004.

Stith, J. L., Avallone, L. M., Bansemer, A., Basarab, B., Dorsi, S. W., Fuchs, B., Lawson, R. P., Rogers, D. C., Rutledge, S., and Toohey, D. W.: Ice particles in the upper anvil regions of midlatitude continental thunderstorms: the case for frozen-drop aggregates, Atmos. Chem. Phys., 14, 1973–1985, https://doi.org/10.5194/acp-14-1973-2014, 2014.

980 Thuman, W. C. and Robinson, E.: Studies of Alaskan Ice-Fog Particles, J. Meteorol, 11, 151–156, https://doi.org/10.1175/1520-0469(1954)011<0151:SOAIFP>2.0.CO;2, 1954.

Um, J. and McFarquhar, G. M.: Single-scattering properties of aggregates of bullet rosettes in cirrus, J. Appl. Meteorol. Clim., 467, 757–775, https://doi.org/10.1175/JAM2501.1, 2007.

Um, J. and McFarquhar, G. M.: Single-scattering properties of aggregates of plates, Q. J. Roy. Meteor. Soc., 135, 291–304, 985 https://doi.org/10.1002/qj.378, 2009.

Um, J. and McFarquhar, G.M.: Dependence of the single-scattering properties of small ice crystals on idealized shape models, Atmos. Chem. Phys., 11, 3159–3171, https://doi.org/10.5194/acp-11-3159-2011, 2011.

Um, J., McFarquhar, G. M., Hong, Y. P., Lee, S.-S., Jung, C. H., Lawson, R. P., and Mo, Q.: Dimensions and aspect ratios of natural ice crystals, Atmos. Chem. Phys., 15, 3933–3956, https://doi.org/10.5194/acp-15-3933-2015, 2015.

990 Um, J., McFarquhar, G. M., Stith, J. L., Jung, C. H., Lee, S. S., Lee, J. Y., Shin, Y., Lee, Y. G., Yang, Y. I., Yum, S. S., Kim, B. G., Cha, J., and Ko, A. R.: Microphysical characteristics of frozen droplet aggregates from deep convective clouds, Atmos. Chem. Phys., 18, 16915–16930, https://doi.org/10.5194/acp-18-16915-2018. 2018.

Waitz, F., Schnaiter, M., Leisner, T., and Järvinen, E.: PHIPS-HALO: the airborne Particle Habit Imaging and Polar Scattering probe – Part 3: Single-particle phase discrimination and particle size distribution based on the angular-scattering function, 995 Atmos. Meas. Tech., 14, 3049–3070, https://doi.org/10.5194/amt-14-3049-2021, 2021.

~~Wang, J. Y., Dong, X. Q., Xi, B. K.: Investigation of ice cloud microphysical properties of DCSs using aircraft in situ measurements during MC3E over the ARM SGP site, J. Geophys. Res. Atmos., 120, 3533-3552, https://doi.org/10.1002/2014JD022795, 2015.~~

Warren, S. G. and Brandt, E. G.: Optical constants of ice from the ultraviolet to the microwave: A revised compilation, J. Geophys. Res. Atmos., 113, D14420, https://doi.org/10.1029/2007JD009744, 2008.

Williams, E.: Thunderstorms and climate., Annual Review of Earth and Planetary Sciences, 46, 421–446, 2018.

Yamazaki, T. and Gonda, T.: Initial Growth Forms of Snow Crystals Growing from Frozen Cloud Droplets, J. Meteorol. Soc. Jpn., 62, 190–192, https://doi.org/10.2151/jmsj1965.62.1_190, 1984.

Yang, P., and Liou, K. N.: Light scattering by hexagonal ice crystals: comparison of finite-difference time domain and geometric optics models., J. Opt. Soc. Am. A, 12, 162–176, https://doi.org/10.1364/JOSAA.12.000162, 1995.

Yang, P. and Liou, K. N.: Single-scattering properties of complex ice crystals in terrestrial atmosphere, Contrib. Atmos. Phys., 71, 223–248, 1998.

Yang, P., Baum, B. A., Heymsfield, A. J., Hu, Y. X., Huang, H. L., Tsay, S. C., and Ackerman, S.: Single-scattering properties of droxtals, J. Quant. Spectrosc. Ra., 79, 1159–1169, https://doi.org/10.1016/S0022-4073(02)00347-3, 2003.

Yang, P., Bi, L., Baum, B. A., Liou, K. N., Kattawar, G. W., Mishchenko, M. I., and Cole, B.: Spectrally consistent scattering, absorption, and polarization properties of atmospheric ice crystals at wavelengths from 0.2 to 100 μm, J. Atmos. Sci., 70, 330–347, https://doi.org/10.1175/JAS-D-12-039.1, 2013.

Zhang, Z. B., Yang, P., Kattawar, G. W., Tsay, S. C., Baum, B. A., Hu, Y. X., Heymsfield, A. J., and Reichardt, J.: Geometrical-optics solution to light scattering by droxtal ice crystals, Appl. Opt., 43, 2490–2499, https://doi.org/10.1364/AO.43.002490, 2004.